MSDE

REVIEW

View Article Online
View Journal | View Issue

Cite this: *Mol. Syst. Des. Eng.*, 2021, **6**, 566

Bioinspired micro/nanomotors towards a self-propelled noninvasive diagnosis and treatment of cancer

Afagh Rastmanesh,†[a] Mohammad Tavakkoli Yaraki, †*[b] Jinyu Wu,[c] Zihao Wang,[c] Prachi Ghoderao,[d] Yongxiang Gao *[c] and Yen Nee Tan *[ef]

The last two decades have witnessed an extensive exploration of micro/nanomotors for an effective biomedical diagnosis and therapy. A nanomotor is a tiny smart device inspired by a biological motor that shows *in situ* energy conversion due to its own movements. Scientists are aiming for more innovative designs of these bioinspired nanomotors towards developing a self-propelled biomedical device that can perform various applications from drug delivery, biosensing to a therapeutic treatment of disease target, where actions can be driven easily by different energy sources, including biochemical, optical, magnetic, and electric fields. Herein, we review the recent development of bioinspired micro/nanomotors for biomedical applications with an aim to better understand the exact mechanism of motor propulsion and to establish a proper command over the motion, direction and speed. Firstly, we highlight energy sources being used for the propulsion of micromotors. Next, we discuss the establishment of micro/nanomotors as an intelligent and comprehensive biomedical nanodevice for the diagnosis and treatment of cancer. Recent studies show that these micro/nanomotors can navigate promptly to target cancer cells, penetrate through the cell membrane, reach up to the cytoplasm and isolate the circulating cancer cells, leading to rapid and ultrasensitive detection. The unique advantages and shortcomings of the differently designed nanomachines are also discussed. Lastly, we present our perspective and highlight the challenges in implementing micro/nanomotors for clinical applications in a real-world environment. It is anticipated that these bioinspired nanomachines/microrobots would be self-propelled and perform multi-tasking, which could help surgeons or physicians to perform challenging and timely tasks for the noninvasive diagnosis and treatment of cancer in future nanomedicine.

Received 1st June 2021,
Accepted 6th July 2021

DOI: 10.1039/d1me00065a

rsc.li/molecular-engineering

Design, System, Application

Biological system has inspired researchers to design tiny structures in the same length scale as biomolecules that could self-propel and move with considerable speed in aqueous solution, termed as "micro/nano motors". Different energy sources including biochemical, optical, magnetic, and electric fields can be used to drive the Brownian motions of these self-propelled nano/micro motors in biological medium. These micro/nanomotors can be designed at the molecular level to allow faster interactions with the biological species, which is important for biomedical applications because faster binding and higher cell uptake of these bioinspired motors would result in earlier detection and stronger therapeutic effects to the diseases cells. This paper reviews the recent advances of the nano/micromotors, which have been successfully employed for both the diagnosis and treatment of cancer including drug/gene delivery and phototherapy. It is envisioned that bioinspiration could be a game changer to the advanced designs of multifunctional intelligent nanomachines/microrobots towards developing a self-propelled non-invasive diagnosis and treatment of cancer with higher precision, accuracy and efficacy in future.

[a] *Department of Materials Science and Engineering, School of Engineering, Shiraz University, Shiraz, 71964-84334, Iran*
[b] *Research and Development Department, Nanofy Technologies Pte. Ltd., 049422, Singapore. E-mail: mohammad@nanofy.co, mty206@yahoo.com*
[c] *Institute for Advanced Study, Shenzhen University, Nanhai Avenue 3688, Nanshan District, Shenzhen 518060, China. E-mail: yongxiang.gao@szu.edu.cn*
[d] *Department of Applied Physics, Defense Institute of Advanced Technology, Pune 411025, India*
[e] *Faculty of Science, Agriculture and Engineering, Newcastle University, Newcastle Upon Tyne NE1 7RU, UK. E-mail: yennee.tan@newcastle.ac.uk*
[f] *Newcastle Research and Innovation Institute, Newcastle University in Singapore, 80 Jurong East Street 21, #05-04, 609607, Singapore*
† A. R. and M. T. Y. contributed equally in this work.

1. Introduction

According to the recent GLOBOCAN 2020 database, the estimated global cancer burden shows 19.3 million newly affected people and 10.0 million deaths in 2020.[1] The rate of recovery from cancer tends to be very low, most likely due to late-stage diagnosis and limited access to timely and standard treatment. The early and accurate diagnosis of cancer is crucial for clinical diagnosis, monitoring its growth, and ultimately for the successful cancer treatment.[2–5] The major challenge of current cancer diagnosis is the lack of specificity in the detection and requirements to perform multiple and invasive diagnostic tests, causing a delay in efficient treatment. Current cancer treatment includes surgical excision of tumors, chemotherapy and/or radiotherapy, either performed individually or in combination. However, all these treatments possess many severe side effects, such as low bioavailability and off-target toxicity.[6] In addition to these existing drawbacks, the antibiotic-resistant nature of a myriad of microorganisms is also responsible for infectious-associated cancers.[7,8] Thus, it is crucial to develop a more efficient and noninvasive methods to solve these complex biomedical challenges. Traditionally, cancer detection is performed by means of conventional tissue biopsy, which involves the removal of a small portion of cells from the primary tumor growth site *via* a surgical procedure followed by the examination of tumor specimens. This poses a significant degree of complication- and injury-related risk to the patient, making it almost impractical to perform repeated biopsies to track disease progression and treatment responses. In addition, there is always a likelihood of clone formation within the tumor,[9–12] which may complicate diagnosis and lead to misleading conclusions with respect to cancer identity. Finally, since tumors are often spatially concentrated in remote parts of the body, such as in the ovaries, pancreas and brain, surgical procedures often need to be performed with a high level of dexterity and precision by highly trained healthcare professionals. This may contribute to the relatively high costs associated with tissue biopsy procedures, making it less affordable to the masses.[13,14]

In the last decades, the field of nanomedicine has received tremendous attention towards improved disease diagnostics, the delivery of therapeutic and imaging payloads, and tissue engineering, among others.[15–20] Considerable efforts have been devoted towards the design of different strategies and nanoplatforms for targeted delivery *in vivo* and probing the cellular function.[21] In nature, the highly efficient biological motors perform complicated tasks by converting fuel, typically adenosine triphosphate (ATP), into mechanical motion. These natural motors are involved in almost every aspect of cell life including division, growth and migration. Inspired by biomotors, scientists from multiple disciplines have focused their research enthusiasm on developing miniaturized motors in an attempt to realize controlled manipulation in the molecular regime. For the controlled motion at a molecular level, sophisticated molecular machines with complex structures, such as molecular cars and molecular elevators, have been engineered. These

Mohammad Tavakkoli Yaraki

Mohammad Tavakkoli Yaraki received his Ph.D. from National University of Singapore under the supervision of Prof Yen Nee Tan and Prof Bin Liu. His Ph.D. thesis was about the synthesis of metal nanoparticles for the plasmonic enhancement study of AIE-based photosensitizers. He is the co-founder of Nanofy Technologies start-up in Singapore. His current research interest is development of hybrid metal nanomaterials for biomedical applications.

Yongxiang Gao

Yongxiang Gao is an Assistant Professor at the Institute for Advanced Study, Shenzhen University. His research interest is on soft matter, with strong focus on developing colloidal model systems and study their self-organization and potential practical use.

Yen Nee Tan

Yen Nee Tan is an Associate Professor and Director of Equality, Diversity, and Inclusion at the Newcastle University (UK) and Newcastle Research & Innovation Institute (Singapore). Her current research focuses on the design and development of multifunctional nanomaterials (e.g., metal, carbon and biohybrids) and smart nanobiosensors technologies inspired by nature for the innovations in chemical/biological analysis, diagnostics, and nanomedicine.

interesting studies and their profound applications have been rewarded with a Nobel Prize for chemistry in 2016. To achieve motion on the nanometer or micrometer scale, profound efforts have been made.[22–25] Recent advances in micro/nanomotor research have rendered them promising tools for addressing many biomedical challenges owing to their unique features, including fast motion, high cargo loading and towing force, and ease of surface functionalization. For example, several motors have already been demonstrated with great potential for targeted drug delivery and cargo release efficiency,[26,27] including self-propelling polymer multilayer nanorockets and TAT peptide-modified stomatocyte nanomotors.[24,25,28–30] Additionally, this new generation of nano/micro motors could be further furnished with bio-smart functions such as pH- and/or temperature responsivity. These smart responsive systems not only can enable faster motion than usual therapeutic nanocarriers but also could selectively interact with the target tissue and timely release of the drug at the target site due to their sensitivity to the change in either temperature or pH of the microenvironment.[31–36]

In this review, we highlight recent advances and prospects in the applications of nano/micromotors for cancer disease diagnosis and therapy with an aim to better understand the exact mechanism of motor propulsion and to establish a proper command over the motion, direction and speed. Firstly, we highlighted the energy sources being used for propulsion of micromotors. Next, we discussed the establishment of micro/nanomotors as intelligent and comprehensive biomedical nanodevices for the diagnosis and treatment of cancer, one of the deadliest illnesses in the world. These include an illustration of the strategies for detecting of cancer biomarkers and the cancer cells using nano/micromotors, as well as the recent advances for the future therapy of cancer through direct cell capture and removal; killing by direct contact or specific drug delivery to the affected site.

2. Principles of micro/nanomotors

2.1. Classification based on the driving force

The motion of a micromotor can always be attributed to some kinds of asymmetry, such as the chemical composition, the shape of the particles and the electric potential gradient around the particles. Based on whether these asymmetries are local or not, we can divide the driving forces of micromotors into internal forces and external forces, respectively. Notably, the propulsion mechanism may not be the only force; instead, it can be a combination of different forces. The internal and external forces could be further classified based on the nature of processes (*i.e.*, chemical or physical) that result in these forces. For example, the motions due to electric or magnetic fields, temperature gradient, concentration gradient, pressure gradient, and viscous forces are all based on a physical process while other motions due to bubble generation (*i.e.*, catalytic, or enzymatic) and electrodeposition are based on the chemical process. In order to design a micro/nanomotor for a specific application, the origin of the forces should be understood.

2.1.1 Internal forces. The typical feature of internal forces is that the driving forces originate from local asymmetry around the particles, such as the self-generated electric potential gradient and chemical potential gradient of solvent species around the particles.

2.1.1.1 Self-generated electric field. Following the phenomenon of electrophoresis, when an electric field is applied to nanoscale or microscale particles in the liquid medium, the particles tend to move towards their respective electrodes. Similarly, some micromotors can generate the local electric potential gradient through chemical gradients of ions and move under their self-generated electric field, which is called self-electrophoresis. The velocity (U) is governed by the following equation:[37]

$$U = \frac{\zeta \epsilon}{4\pi\eta} E \tag{1}$$

where ζ is the zeta potential of the particles, ϵ is the permittivity of the medium, η is the viscosity of the medium, and E is the electric field at the outer edge of the double layer.

Micromotors driven by self-electrophoresis are mostly bimetallic. The first micromotor was discovered by Paxton *et al.* It was rod-shaped, with half-gold (Au) and half platinum (Pt) fabricated through the template-based electrodeposition method using AAO (anodized alumina oxide) membranes (Fig. 1a).[38] The as-obtained bimetallic rods (2–3 μm in length and about 300 nm in diameter) could move with a speed of about 10 μm s^{-1}. The shape of bimetallic micromotors is not limited to rod-like shape. For instance, Wheat *et al.* have fabricated bimetallic Janus spheres (Fig. 1b) using the sputter coating method,[39] where the entire surface of polystyrene microspheres was coated with platinum followed by half-coating of gold on these platinum-coated spheres. This study found that a 3 μm diameter micromotor is capable of moving at about 15 μm s^{-1} (Fig. 1b).

2.1.1.2 Concentration gradient of neutral species. The dipole and Van Der Waals interactions between the neutral solute molecules and the surface of colloidal particles lead to the motion of colloidal particles. This phenomenon is classified as diffusiophoresis or osmosis of neutral solutes.

The slip velocity is given by the following formula by Anderson *et al.*[37]

$$v_s = -\frac{kT}{\eta} KL \times \nabla c \tag{2}$$

$$K = \int_0^\infty \left[\exp\left(-\frac{\Phi}{kT} \right) - 1 \right] dy \tag{3}$$

$$L^* = K^{-1} \int_0^\infty \left[\exp\left(-\frac{\Phi}{kT} \right) - 1 \right] dy \tag{4}$$

Here, k is the Boltzmann constant, T is the temperature, η is the viscosity of the medium, Φ is the potential energy of a

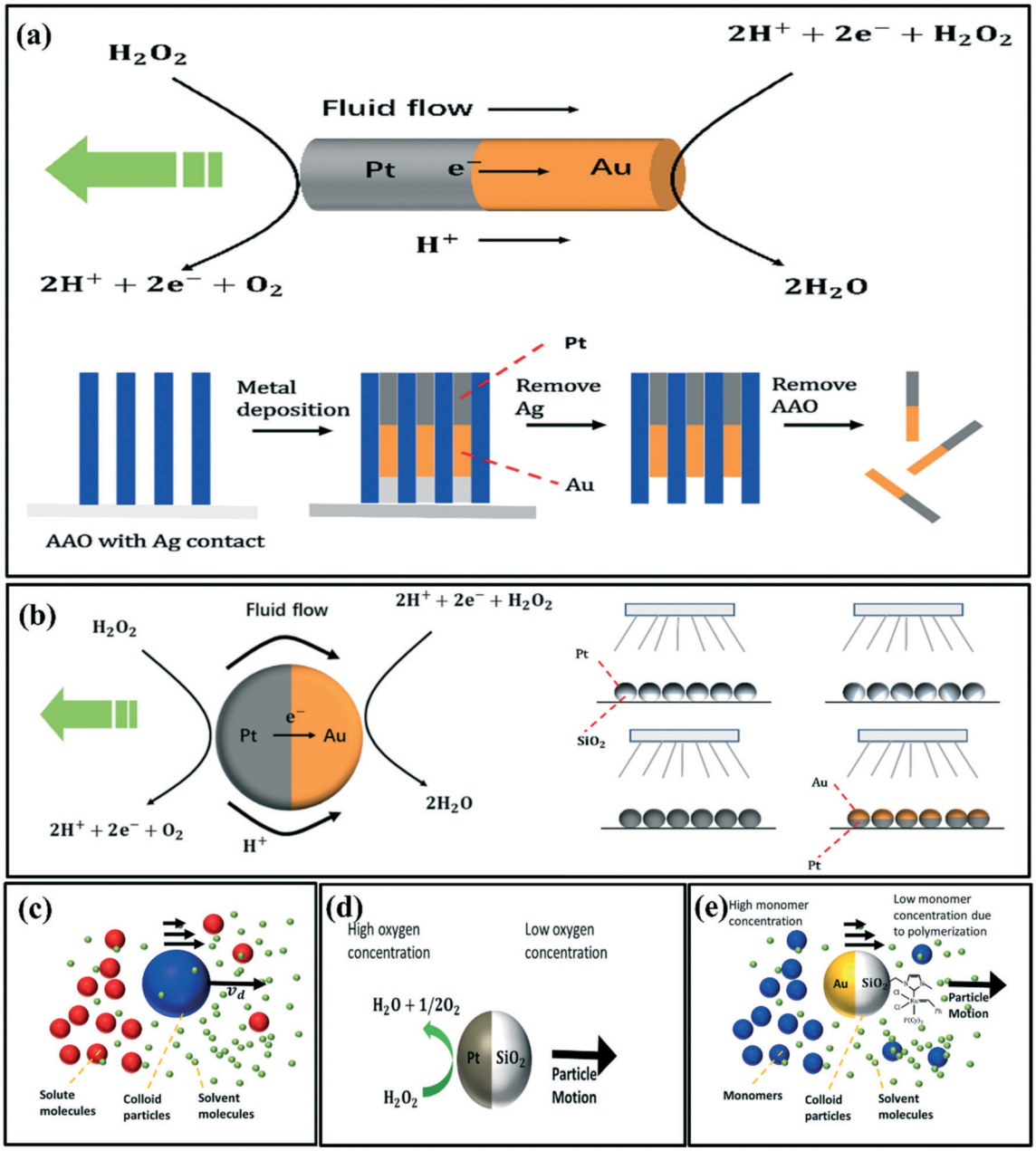

Fig. 1 Schematic diagrams of the (a) electrophoresis of Au–Pt rods and the template-based electrodeposition process, reproduced with permission from ref. 38, (b) electrophoresis of Au–Pt spheres and the fabrication method to form the Au–Pt Janus particles, reproduced with permission from ref. 39 (c) self-diffusiophoresis of neutral species, (d) self-diffusiophoresis of Pt–SiO_2 microspheres, reproduced with permission from ref. 40, (e) self-diffusiophoresis of Au–SiO_2 microspheres modified with the Grubbs'catalyst on the SiO_2 side, reproduced with permission from ref. 41.

solute molecule at a distance y from the particle surface, K the Gibbs adsorption length, which describes the amount of adsorbed solute per area of surface divided by the equilibrium concentration, and L^* is the characteristic length for the particle–solute interaction. With the known shape and chemical properties of colloidal particles, Φ and v_s can be theoretically calculated, and the diffusiophoretic velocity is given by $v_d = -v_s$.

Fig. 1c illustrates the self-diffusiophoresis process of neutral species. The key for diffusiophoresis of neutral species is to generate the local concentration gradient around the particles, either by increasing or decreasing the solute concentration asymmetrically. For example, Ma *et al.* have fabricated Janus Pt–SiO_2 microspheres by depositing a thin Pt layer to a monolayer of SiO_2 microspheres. The Janus Pt–SiO_2 micromotors propel by increasing the O_2 concentration at the Pt end (Fig. 1d).[40] Pavlick *et al.*[41] have observed the self-diffusiophoresis of Janus Au–SiO_2 microspheres, which have been modified with the Grubbs' catalyst on the SiO_2 side. The Grubbs' catalyst has high polymerization activity

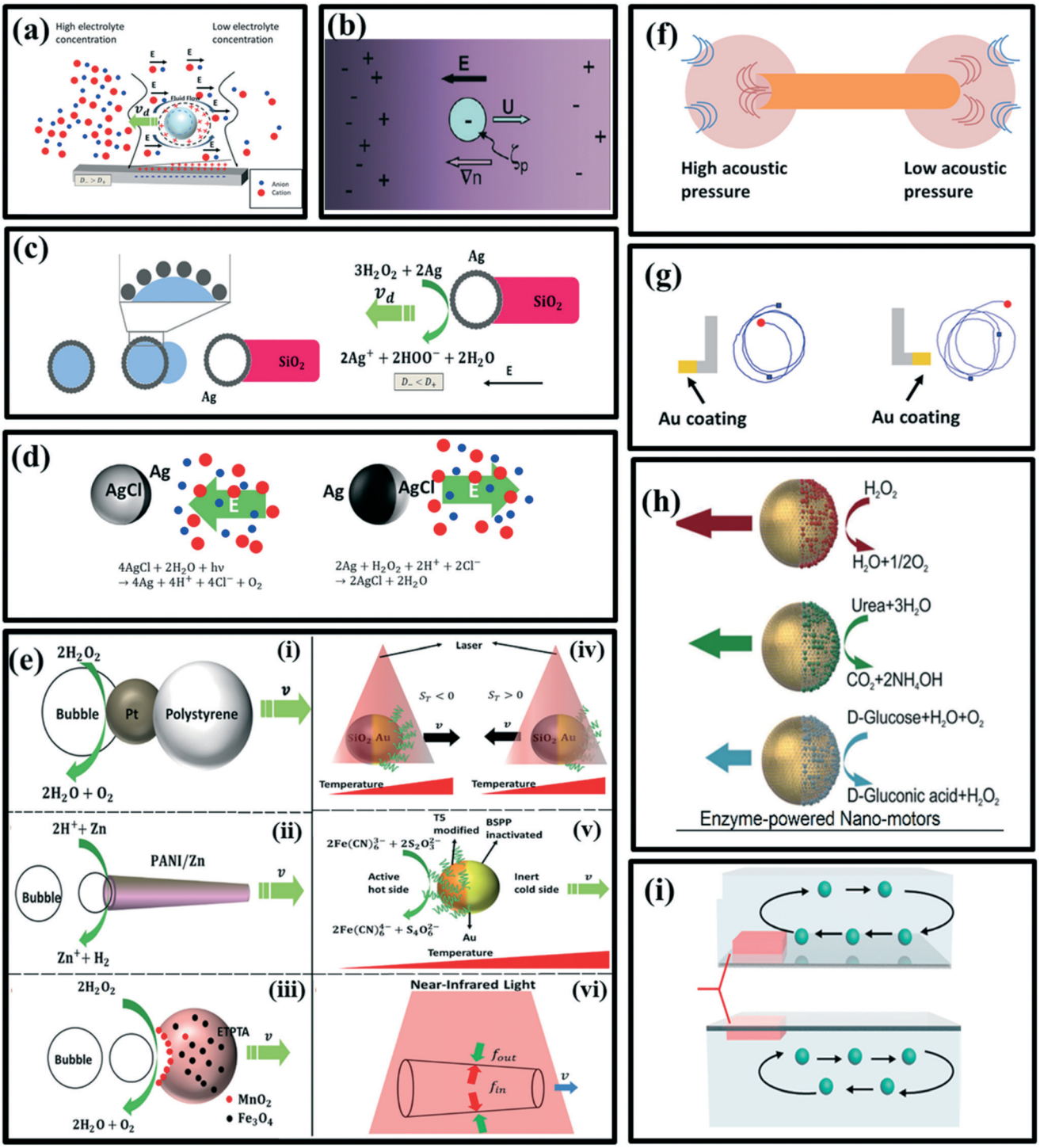

Fig. 2 Schematic illustration of the (a) self-diffusiophoresis of electrolyte, reproduced with permission from ref. 49, (b) self-diffusiophoresis of Ag-Dynabead microspheres, reproduced with permission from ref. 42, (c) the bulk synthesis method of Ag–SiO_2 rod-like micromotors and self-diffusiophoresis of Ag–SiO_2 rod-like micromotors, reproduced with permission from ref. 43, (d) oscillation of AgCl particles due to reversible conversion of AgCl to Ag at the surface, reproduced with permission from ref. 44, (e) (i) O_2 bubble propelled Pt-polystyrene dimer, reproduced with permission from ref. 50, (ii) H_2 bubble propelled zinc-based microtube, reproduced with permission from ref. 47, (iii) O_2 bubble propelled ETPTA/Fe_3O_4/MnO_2 crescent micromotor, reproduced with permission from ref. 48, (iv) self-thermophoresis of Au/SiO_2 Janus sphere, reproduced with permission from ref. 51, (v) catalysis driven self-thermophoresis of Janus Au NPs, reproduced with permission from ref. 52, (vi) the $(PSS/PAH)_{20}$ Au NS microtube driven by the temperature gradient, reproduced with permission from ref. 53. (f) Self-acoustophoresis driven bimetallic Au/Ru rod, reproduced with permission from ref. 54, (g) L-shaped micro-motors and their trajectories, reproduced with permission from ref. 55, (h) Janus hollow mesoporous silica nanoparticles and reactions of biocatalyze enzymes, reproduced with permission from ref. 56, (i) simulation image of thermoconvective flow (inward flow and outward flow), reproduced with permission from ref. 57.

with norbornene, and hence it decreases the monomer concentration at the silica side (Fig. 1e).

2.1.1.3 Concentration gradient of electrolyte. The self-diffusiophoresis of a charged solute arises from the combination of two mechanisms. One of them is quite similar to the self-diffusiophoresis of neutral species, as shown in Fig. 2(a). While the other one is typically based on the self-generated electric field due to the difference in diffusion coefficients of the positive and negative ions. Thus, the velocity v_d is a composition of electrophoretic and chemophoretic terms[37] as follows.

$$v_d = -v_s = \frac{\epsilon\zeta}{4\pi\eta}\left(\frac{kT}{Z_e}\right)\frac{D_+ - D_-}{D_+ + D_-}\frac{\nabla c}{c_0} - \frac{\epsilon}{2\pi\eta}\left(\frac{kT}{Z_e}\right)^2 \ln\left(1-\xi^2\right)\frac{\nabla c}{c_0} \quad (5)$$

where $\xi = \tanh\left(\frac{z\epsilon\zeta}{4kT}\right)$, ζ is the zeta potential of the particles, ϵ is the permittivity of the medium, η is the viscosity of the medium, k is the Boltzmann constant, T is the temperature, Z_e is the absolute charge carried by the electrolyte ions, D_+ and D_- are the diffusivity of the cations and anions, respectively, c is the local concentration and c_0 is the bulk concentration of ions. The self-diffusiophoresis of electrolytes is shown schematically in Fig. 2a. Similar to neutral species, micromotors change the local electrolyte concentration through chemical reactions. The commonly used substrates include silver and silver salts such as AgCl. Chaturvedi *et al.* have synthesized Ag-Dynabead heterodoublet micromotors (Fig. 2b).[42] The study showed that heterodoublet micromotors generate ions at the Ag end, which subsequently, develop a concentration gradient of electrolyte. The magnetic field was used to decide the direction of the micromotors. Further, rod-like micromotors have also been studied. Gao *et al.* have developed a bulk synthesis method for Ag–SiO_2 rod-like micromotors and found that these are more efficient than currently available micromotors (Fig. 2c).[43] Ibele *et al.* have shown that the oscillations of AgCl particles occur due to two main factors, a reversible conversion of ions at the surface and the self-diffusiophoresis mechanism (Fig. 2d).[44]

2.1.1.4 Bubbles. Asymmetric generation of bubbles around the particles is also a possible propulsion mechanism. Gibbs *et al.* have raised a simple model to understand the driving force: the detachment of bubbles with an initial velocity leads to a non-zero driving force on the particles due to momentum conservation.[45] The driving force can be expressed as a function of horizontal velocity v as below:

$$F_{drive} = N\frac{\nabla m}{\nabla t}(v_0 - v) \quad (6)$$

Here N is the number of bubbles separated from the particles, Δm is the mass change due to a single bubble, Δt is the average time for bubbles to grow until detachment, which depends on the catalytic reaction and the shape, and v_0 is the initial horizontal speed of the detached bubble. Since the motion is discontinuous due to the release of bubbles, we can roughly estimate the average speed as the speed when the viscous force and driving force reach equilibrium, *i.e.*, $F_{drive} = F_{drag}$, where F_{drag} depends on the shape of the motors, viscosity of the fluid and the speed of the particles. From the relation above, we can calculate the estimated speed of the motors.

Compared to the self-electrophoresis and self-diffusiophoresis-driven micromotors, which usually propel with approximately several microns per second, bubble-driven micromotors can reach the speed of hundreds of microns per second, which is ultrafast. For reaction generating gas molecules, it is possible for both self-diffusiophoresis and bubble propulsion mechanisms. For example, Wang *et al.* have shown that Pt-catalyzed decomposition of hydrogen peroxide can also produce bubble propulsion, but they have used a chemical deposition method to fabricate a Pt-polystyrene dimer instead of the physical coating method (Fig. 2e(i)).[50] Other bubble-propelled micromotors include some well-designed shapes such as microtubes[46] (Fig. 2e(ii)) and crescent shape,[47] which cleverly control the release site of the bubbles (Fig. 2e(iii)).[48]

2.1.1.5 Gradient of temperature. The gradient of temperature is just like the concentration gradient, it can also lead to the motion of microparticles in the fluid, *via* a mechanism called self-thermophoresis. The propulsion velocity can be expressed as follows.[37]

$$v = -v_s = \frac{2}{\eta}\int_0^\infty y h(y)\mathrm{d}y\frac{\nabla T}{T_0} \quad (7)$$

where η is the viscosity of the medium, y is the distance from the particle surface, $h(y)$ is the local excess-specific enthalpy (erg cm^{-3}) in the interfacial layer compared with the bulk fluid, T is the local temperature and T_0 is the bulk temperature.

Jiang *et al.* have irradiated Au–silica spherical Janus particles with a laser, Au-coated hemisphere absorbs the laser and consequently, the self-thermophoresis phenomenon take place to drive the motors (Fig. 2e(iv)).[51] However, Qin *et al.* have used a catalyzed redox reaction to generate heat at the active hot site of Janus Au nanoparticles (NPs). The first half of an Au nanoparticle was modified with a short thiolated oligonucleotide (T5), which remains catalytically active, while the other half was inactivated by bis(*p*-sulfonatophenyl) phenyl-phosphine (BSPP) (Fig. 2e(v)).[52] Wu *et al.* have shown that a (poly styrenesulfonic acid/poly allylamine hydrochloride)$_{20}$ Au nanoshells' microtube having an opening at both ends of different sizes can also be propelled by the self-generated temperature gradient (Fig. 2e(vi)).[53]

2.1.1.6 Acoustically generated pressure gradient. Since ultrasonic sound is already being widely used in medical diagnosis and therapeutics, scientists have also focused their eyes on ultrasonic energy as a driving force in micro-motors. Wang and coworkers have discovered that the asymmetric micro-rods with a concave end and a convex end can scatter the acoustic waves differently, leading to the generation of pressure difference at both ends of microrods (Fig. 2f).[54] This

mechanism is called self-acoustophoresis; unfortunately, it has not been well studied and understood yet.

2.1.1.7 Viscous force due to asymmetric shape. The circular motion has also attracted scientists' attention as it is one of the most fundamental motions occurring in nature. Kümmel *et al.* have produced L-shaped micromotors with Au-coated short arms, which become hot upon illumination of light, and turn into a self-phoretic motion. This research group has reported that a velocity-dependent torque induced by viscous forces plays a vital role in performing circular motion by the asymmetric micro-motors (Fig. 2g).[55]

2.1.1.8 Enzyme-driven motion. Another driving mechanism being used is an enzyme-powered motion. The micromotor powered by enzymes has been privileged with specific characteristics such as non-toxicity, high reaction rates and multiple choices of enzyme/fuel combinations. The biocompatibility of enzymes also makes them more applicable in the biological environment. Generally, enzymes such as lipase, urease and glucose oxidase (GOX) are being used. Catalase is efficient but in some conditions, it can show some side effects. The nanomotor can also be employed as a vehicle for drug delivery with controlled release of drug molecules at the target-specific site by using chemotaxis, pH taxis, and/or remote magnetic guidance. Ma *et al.* have reported the use of asymmetric biocatalytic reactions, to produce a gradient of the chemical species driving the active motion of nanomotors (Fig. 2h).[56] A formula for the study of force acting on the nanomotors is shown in eqn (8). It is an absolute driving force for a spherical particle with two rotational degrees of freedom.

$$F = \frac{3k_B T}{2r}\sqrt{2\left(\frac{D_L}{D_t} - 1\right)} \tag{8}$$

It's an absolute driving force for a spherical particle with two rotational degrees of freedom.

In the glucose-powered micromotors, glucose oxidase (GOX) catalyzes the decomposition of glucose into gluconic acid and hydrogen peroxide (H_2O_2). Zhang *et al.*[57] have hypothesized that a glucose-powered micro-pump makes thermo-convective flow, which further leads to the motion of the micropump (Fig. 2i). They have characterized the speed of the flow as follow,

$$V = \frac{g\beta h^3 r\Delta H}{\nu\kappa\pi R(R + 2l)} f(a, b) \tag{9}$$

g, h, β, ν, κ represent the gravitational acceleration, the thickness of the liquid layer, the coefficient of thermal expansion, kinematic viscosity, thermal conductivity of the liquid, respectively, and r, ΔH being the rate, and enthalpy of the chemical reaction, respectively. R and l are the radius and height of the gel. $f(a, b)$ depends on the aspect ratios of the micro-pump, $a = R/h$ and $b = l/h$. The urea-powered nanomotor catalyzes the decomposition of urea into CO_2 and

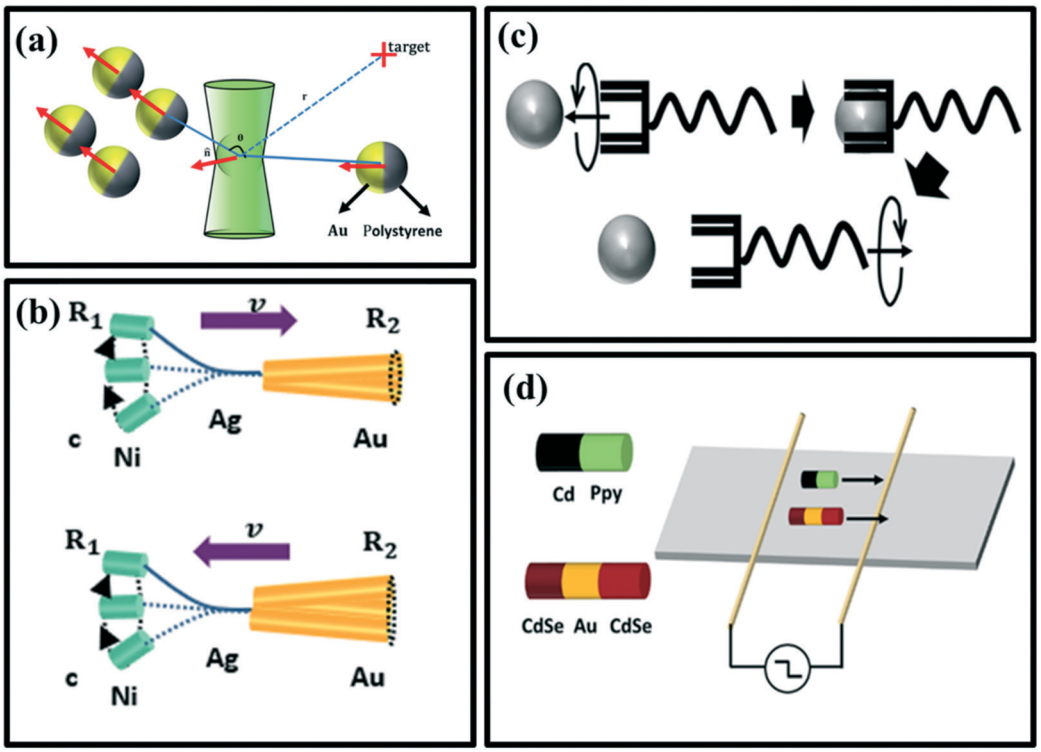

Fig. 3 (a) The manipulation of Au-PS Janus microspheres by adaptive photon nudging, reproduced with permission from ref. 60, (b) movement of rigid Au/Ag/Ni (top) and flexible Au/Agflex/Ni (bottom) nanowires under a rotating magnetic field, reproduced with permission from ref. 61, (c) transportation procedure of a helical micromachine, reproduced with permission from ref. 62, (d) propulsion of PPy/Cd and CdSe–Au–CdSe nanowire under AC electric field diodes, reproduced with permission from ref. 63.

NH_3. Ma *et al.* have formulated Janus hollow mesoporous silica microparticles, which have been powered by the biocatalytic decomposition of urea at physiological concentrations.[58] It has been observed that the microparticles have moved for a longer time with higher speed. Moreover, the speed and direction of the particles can be controlled

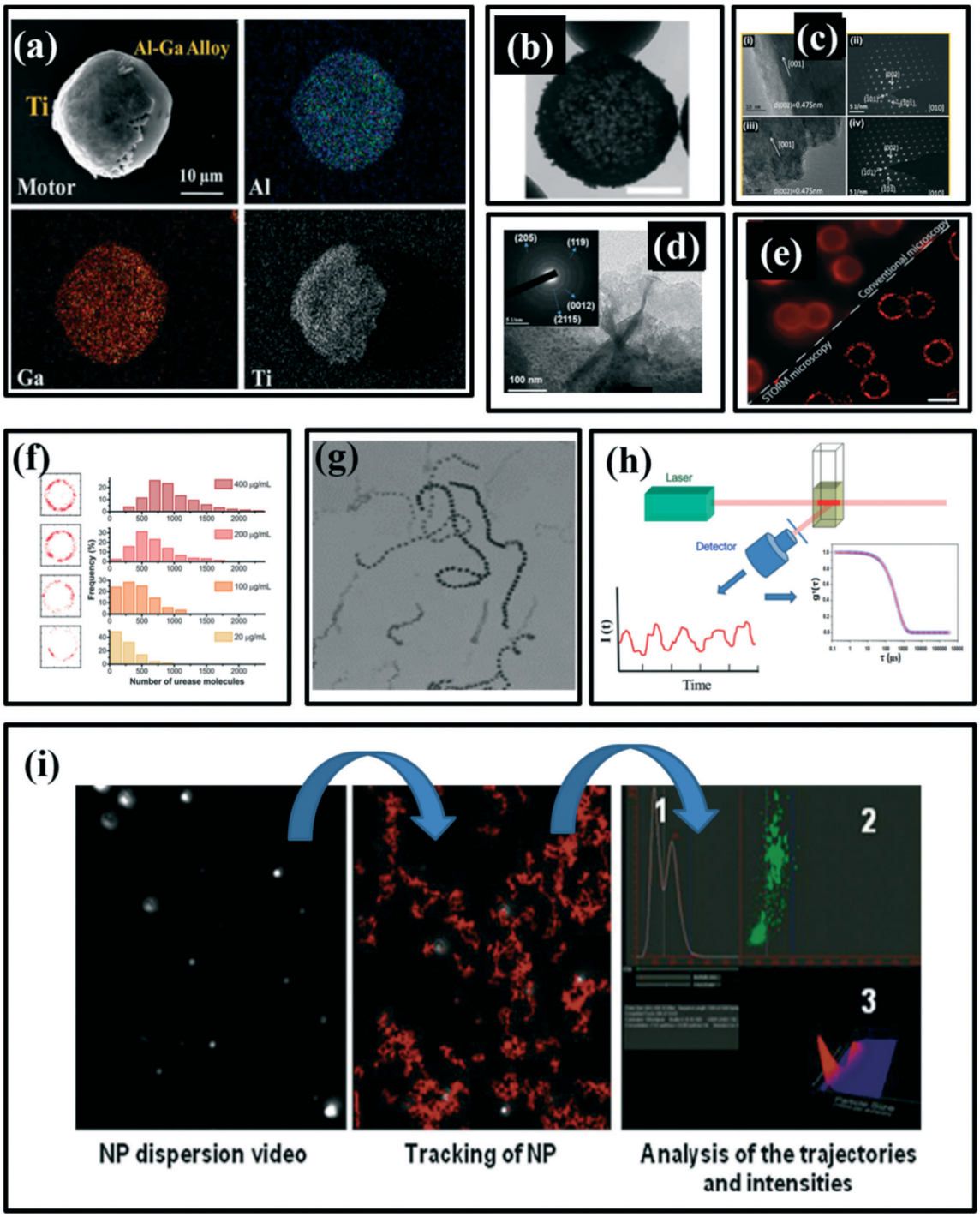

Fig. 4 (a) SEM image of Janus Al–Ga/Ti micro-motors and the corresponding energy-dispersive X-ray spectroscopy (EDX) show the element distribution of Ga, Al and Ti, reproduced with permission from ref. 64, (b) the TEM image of the head of a rod-like micromotor, reproduced with permission from ref. 43, (c) HRTEM images (i, iii) and SAED patterns (ii, iv) at three locations along the TiO_2 nanorods, reproduced with permission from ref. 65, (d) TEM images and SAED patterns at three locations along the TiO_2 nanorods, reproduced with permission from ref. 66, (e) red circle is the urease conjugated with particles, reproduced with permission from ref. 67 (f) number of urease molecules on a nanoparticle, reproduced with permission from ref. 67, (g) optical image of a self-propelled motion of silver/silica motors, reproduced with permission from ref. 43, (h) typical analysis procedure of DLS, reproduced with permission from ref. 68, (i) typical image produced by nanoparticle tracking analysis (NTA), reproduced with permission from ref. 69.

efficiently by commanding the enzymatic activity of urease and the applied magnetic field.

2.1.2 External forces. As compared to internal forces, the external forces, including light, magnetic field and electric field are also being used with the additional benefit that these forces can be controlled mechanically.

2.1.2.1 Radiation-pressure forces. Although light can also induce self-generated temperature gradient, as with other external forces, here, we have mainly focused on the radiation-pressure forces. According to Roosen *et al.*,[59] the radiation-pressure force on a particle by a ray of light at a particular angle is,

$$F_R = (A + 2R)I_0 \left(\frac{C}{n_m}\right)^{-1} \hat{k} \quad (10)$$

where A and R are the total absorbance and reflectance of the system, I_0 is the light intensity, c is the speed of light, $\hat{k}$ is the light propagation direction. The net force can be calculated by integrating over the area swept by the laser. Usually, radiation-pressure forces come together with self-thermophoresis to propel micromotors. For example, Qian *et al.* have used adaptive photon nudging to manipulate the motion of Au-PS Janus microspheres (Fig. 3a).[60]

2.1.2.2 Magnetic field and electric field. External magnetic and electric fields can also propel micromotors. Gao *et al.* have used a magnetic field to propel a flexible metal nanowire micromotor (Fig. 3b),[61] and a helical micromachine was studied by Tottori *et al.* to get in-depth knowledge regarding the transportation procedure in the cells (Fig. 3c).[62] Calvo-Marzal *et al.*[63] have skillfully illustrated that PPy–Cd and CdSe–Au–CdSe Schottky barrier diode nanowires can be propelled controllably by applying the uniform AC electrical field (Fig. 3d).

2.2. Characterization of micro/nanomotors

2.2.1 Particle characterization. Micro/nanomotors are usually in the size range of nanometers to micrometers. Hence, for the assessment of the size and shape of the micromotors, characterization techniques such as scanning electron microscopy (SEM), energy-dispersive X-ray spectroscopy (EDX), and transmission electron microscopy (TEM) can be used. SEM can reveal the topography of the sample, including size and shape with higher resolution. An SEM equipped with EDX can produce characteristic X-rays, giving information about the abundance of elements in the sample as well as mapping the elemental distribution. In Fig. 4a, an SEM image of Janus Al–Ga/Ti micromotors by Gao *et al.*[64] has been shown along with the corresponding EDX, which has confirmed the element distribution of Ga, Al and Ti. TEM is another more precise technique in nanomaterial studies. It can reveal the internal structure of the nanosized sample, including the presence of atoms and their bonding. For example, Fig. 4b shows the TEM image of the head of a rod-like micromotor.[43]

Selected area electron diffraction (SAED) patterns can recognize the crystal structures and measure the lattice parameters of particles. It also has the ability to identify the configuration and distinguish nanocrystalline from similar phases. Fig. 4c shows HRTEM images (i, iii) of high-quality TiO_2 nanorods. Further, the phase purity of the anatase TiO_2 nano-rods has been observed by SAED patterns (ii, iv) at two different locations along the TiO_2 nanorods.[65] Liu *et al.*[66] have used the SAED patterns to show four different crystal patterns, which are indicative of multiple crystallographic orientations corresponding to the mixed structures of MnO_2 and Mn_2O_3 (Fig. 4d).

Stochastic optical reconstruction microscopy (STROM) is also a particle characterization technique mainly used to quantify the number of enzymes. Patiño *et al.*[67] have confirmed the conjugation of enzyme onto nanomotor as shown in Fig. 4e, and the quantity of the enzymes conjugated nanomotor has been observed in Fig. 4f.

2.2.2 Motion characterization. For large and opaque micro/nanomotors, an optical microscope is the easiest technique to monitor the motion of these motors. For example, Gao and coworkers have tracked and analyzed the motion of silver/silica motors using an optical microscope (Fig. 4g).[43] However, as the nanoparticles have a refraction index closer to water (solvent), an optical microscope does not work. Instead, dynamic light scattering (DLS) and nanoparticle tracking analysis (NTA) are more useful techniques to characterize the motion of nanoparticles (Fig. 4h and i).[68,69] In NTA, the individual position is tracked as a video, from which the motion can be analyzed. While in DLS, instead of individual particle tracking, the time-dependent scattering intensity fluctuations can be detected, and the average particle size, as well as a polydispersity index, can be calculated. The fluorescence imaging technique is also being used commonly. However, it has some limitations such as the need for organic dyes, quantum dots, or fluorescent polymer dots as the fluorescent probe, which are mostly toxic, difficult to modify on the surface, and exhibit poor photostability in aqueous environments.

Recently, there are also interesting advances in optical imaging with anisotropic plasmonic nanoparticles.[70] Based on the remarkable optical properties related to the localized surface plasmon resonance (LSPR) of plasmonic nanoparticles, scientists have developed various optical imaging methods with anisotropic plasmonic nanoparticles, which include dark-field microscopy, total internal reflection scattering microscopy, differential interference contrast microscopy (DIC), two-photon luminescence imaging (TPL) microscopy, *etc.* The DLS technique take advantages of the size-dependent Brownian motion to characterize the nanoparticles' hydrodynamic size by measuring their inherent diffusion coefficient based on the Stokes–Einstein equation. This technique has been used to develop ultrasensitive nanosensors for cancer diagnostic and other related diseases.[5,71]

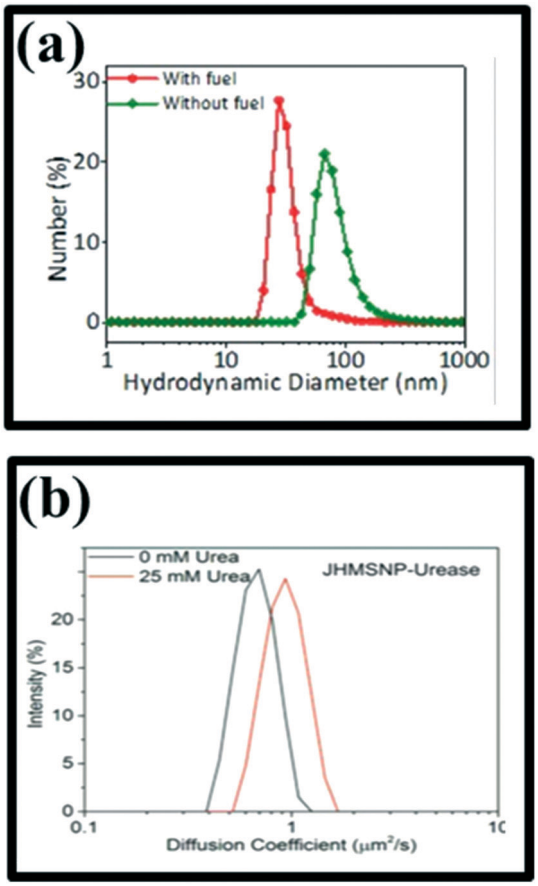

Fig. 5 (a) Nanorocket size distribution as measured by DLS, reproduced with permission from ref. 72, (b) diffusion coefficient histogram of two nanomotors measured by DLS, reproduced with permission from ref. 56.

$$D_{\text{eff}} = \frac{Tk_{\text{b}}}{3\pi\eta d} \tag{11}$$

where $k_{\text{b}}T$ is the thermal energy, η is the kinematic viscosity, and d is the hydrodynamic diameter. Li *et al.*[72] have measured nanorocket size distribution using DLS (Fig. 5a). Subsequently, Ma *et al.*[56] have measured the relationship between intensity and diffusion coefficients using the same machine (Fig. 5b).

Magnetic resonance imaging (MRI) is also a tracking method, used to locate the ferromagnetic core of uncontrolled microdevice or nanorobot for navigation or closed-loop control purposes. It is deeply related to the application of radio frequency (RF) excitation signals, which are adjusted to the equipotential magnetic curve generated by the magnetic signals of the tracked object. In order to obtain a 3-D location of the device, a correlation function on just one *k*-space line for its *x*, *y*, *z* axes is used, which corresponded to three projections. There are three categorized methods to track the inserted device, *i.e.*, passive, semi-active, and active. The passive method uses the susceptible difference between the background and the inserted devices. Semi-active methods are quite similar to passive methods except that they need external ways to control the signal loss caused by susceptibility differences. Active methods apply projections to give superior spatial and temporal resolutions, but it needs an antenna to be added to the scanner. Felfoul *et al.*[73] have tracked the ferromagnetic spheres using the MRI technique and compared the data with the data obtained from the camera. The average positioning error is approximately 0.6 mm.

3. Cancer diagnostics

The effectiveness of cancer treatment strongly depends on the accuracy and stage of diagnosis of cancer. Therefore, early screening of tumors is of great importance and plays a significant role in the treatment of various cancers, in particular, breast and cervical cancer in women as well as prostate and colon cancer in men. Prevalent methods of cancer diagnosis today mainly include body fluid analysis tests, medical imaging, biopsy, and biomarker monitoring. Most of these methods are not accurate enough to diagnose most types of cancer in the early critical stages. That is why cancer is usually detected with delay when the tumor size is larger than the acute level that ultimately makes the treatment more difficult in these conditions.[74,75]

To overcome the failure of the treatment due to delayed or inaccurate diagnosis, micro/nanomotors are being used as these motors show a more affirmative and precise detection of the disease. The faster mobility of micro/nanomotors as compared with the conventional diagnostic nanomaterial probes, allows them to not only interact with more analyte molecules in a shorter time and increase the sensitivity but also enables the higher tissue penetration for *in vivo* diagnosis.[76] Thanks to the recent advances in the field of micro/nanomotors, research made these motors highly biocompatible rendering them promising candidates for the future of diagnosis and nanomedicine.[77–80] In the subsequent sections, we will discuss the recent advancements in the application of micro/nanomotors for accurate detection of cancer biomarkers and cancerous cells (Table 1).

3.1. Cancer biomarker detection

A biomarker is a measurable substance or activity that can represent a natural biological process, a pathogenic process, or a drug response to the therapeutic interaction. Cancer biomarkers are found in tumor tissue or serum and include various molecules, including DNA, mRNA, enzymes, metabolites, cell surface receptors, and proteins. Developing sensitive, selective, reliable and cost-effective diagnostic solutions and methods for cancer risk assessment, early detection, and classification of tumors is emerging so that the patient can receive the best and most effective treatment, while physicians can observe the progress, relapse, and recurrence of the disease.[81,82] Over the past few decades, significant progress has been made in this area. Numerous diagnostic methods have been developed based on intracellular biomarkers or DNA/protein biomarkers on the

Table 1 Representative examples of cancer biomarker and intracellular detection using micro/nanomotors

Micro/nanomotor	Driving force	Recognition element	Analyte	Medium	Linear range	Limit of detection	Ref.
rGO/Pt microtubes	H_2O_2	Reprimo/FAM	Reprimo ssDNA	TE buffer solution	1–10 (μM)	1.3 (μM)	98
(AuNP/PANI/Pt)@Ab-GMA	H_2O_2	Capture antibody-GMA	Carcinoembryonic antigen	Serum	1–1000 ng mL^{-1}	—	101
SiO_2/Au/Ag/Ni/Au@MCH/silica	H_2O_2	DNA and catalase	DNA	Serum and cell culture	25–750 nM	—	99
MnO_2–PEI/Ni/Au	H_2O_2	$Aptamer_{KH1C12}/Au_{nano}$-PEDOT/GC electrode	HL-60	Human serum	2.5×10^1–5×10^5 cells per mL	250 cells per mL	103
Au–PtNP-peptide-PEG	NIR and H_2O_2	Tumor-targeted peptide and poly(ethylene glycol)	Tumor cells	HeLa cells	—	—	108
MHSNP/Pt/F	NIR	EpCAMAb	CTC	Whole blood	—	—	102
ssDNA@GOmodified AuNWs	Ultrasound	Dye-ssDNA/graphene-oxide	miRNA-21	MCF-7 and HeLa cells	—	—	107
FAM-AIB1-aptGO/AuNW	Ultrasound	FAM-AIB1-aptamers	AIB1 oncoprotein	MCF-7	—	—	110
FAM-ssDNA-GO-AuNW	Ultrasound	FAM-ssDNA	HPV16 E6 mRNA	Cell culture	—	—	111
SH-DP-Ag NPs	H_2O_2	DNA	*E. coli* 16S rRNA	*E. coli* lysate solutions	40 amol–400 fmol	Variable	112
PEDOT/Au microtube	Bubble-induced/H_2O_2	DNA	DNA	Cell culture	—	1 pmol	113
USSN	H_2O_2	Catalase enzyme	Hela cells	DMEM buffer	—	—	109

Abbreviations: rGO: reduced graphene oxide, FAM: fluorescein amidine dye, NP: nanoparticles, PANI: polyaniline, GMA: glycidyl methacrylate, Ab: antibody, MCH: 6-mercapto-1-hexanol, HER2: human epidermal growth factor receptor 2, MHS: magnetic hierarchical silica, NIR: near-infrared, CTC: circulating tumor cells, EpCAM: epithelial cell adhesion molecule, NW: nanowire, PEI: polyethyleneimine, PEDOT: poly(3,4-ethylene dioxythiophene), USSN: ultrasmall stomatocyte nanomotors, DMEM: Dulbecco's modified Eagle's medium, DP: detector probe.

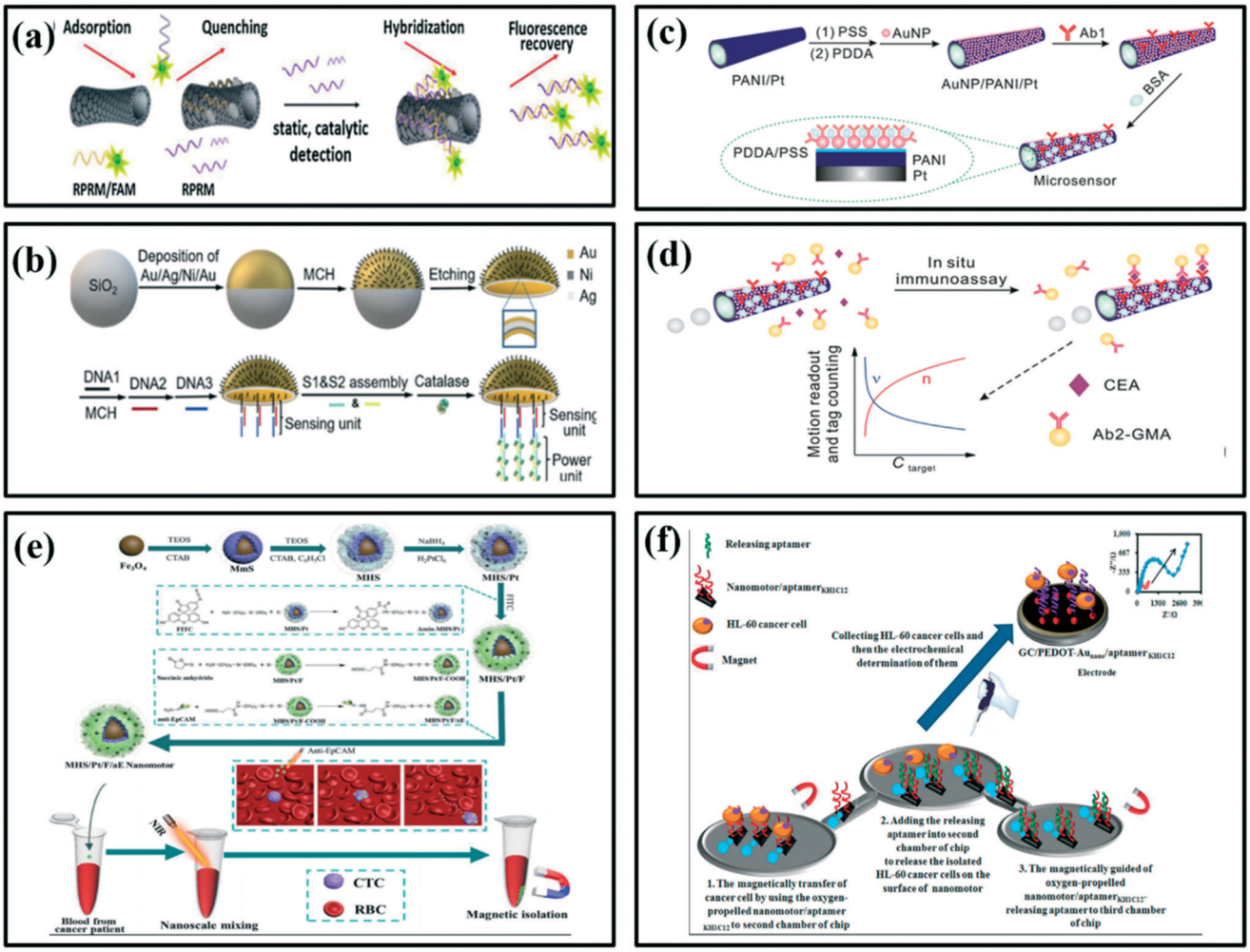

Fig. 6 Schematic illustration of the (a) fluorescent detection strategy for Reprimo, a gastric cancer biomarker, using nanomotors, reproduced with permission from ref. 98, (b) fabrication of the jellyfish-like micromotor, reproduced with permission from ref. 99, (c) fabrication of motor-based microsensor, reproduced with permission from ref. 101 and (d) use for *in situ* protein biomarker detection *via* motion readout and tag counting, reproduced with permission from ref. 101, (e) construction of NIR-driven fluorescent magnetic nanomotors and their application for the capture of circulating tumor cells (CTCs), reproduced with permission from ref. 102, (f) sensing principle for HL-60 cancer cell determination, reproduced with permission from ref. 103.

surface of disease/cancer cells,[4,83,84] including polymer chain reaction (PCR), enzyme-linked immunosorbent assay (ELISA), microcontrollers, colorimetric method,[3,85–89] electrochemical method, light scattering,[71,90] and fluorescent methods.[91–94] Although these methods are very effective, some of them do not have the sensitivity and precision required for medical diagnostic applications. However, micro/nanomotors have functional features such as active mobility and controllability that make them a viable option for detecting cancer biomarkers.[81]

DNA is a unique biomacromolecule with great self-assembly properties and one of the most important biomarkers for several diseases and cancer.[95–97] For example, self-propelled electrochemically reduced graphene oxide and Pt (rGO/Pt) microtubes were used to detect a gastric cancer biomarker, Reprimo, through the off/on fluorescence, as shown in Fig. 6a. Detection was done *via* a hybridization process between the Reprimo probes tagged with a fluorescein amidine dye (FAM) and the target biomarker Reprimo ssDNA, followed by detachment from microtubes. Upon the addition of target RPRM, the hybridization process takes place, releasing double-stranded from the microtube to allow recovery of fluorescence intensity from the FAM dye for biomarker detection. The catalytic motion of the designed micromotor showed that they can reach fast speeds of up to 360 μm per second (s) in the presence of H_2O_2 as fuel, while the limit of detection for Reprimo was 1.3 μM.[98]

In another work for DNA detection, a jellyfish-like micromotor with a multimetallic shell deposited on a SiO_2 microsphere was designed by Zhang *et al.*[99] As shown in Fig. 6b, the jellyfish-like micromotor was decorated with self-assembled DNA and catalase, which can be used for sensing applications. It showed great sensitivity, stability and good bubble-propelled mobility with speeds up to 209 μm s^{-1}

through the H_2O_2-induced catalytic motion. Under optimal conditions, the relationship between the movement speed of the micromotors and the concentration of the target DNA was studied. An inverse linear correlation with the concentration of the target DNA and the speed signal was obtained. In the presence of target DNA, catalase was released from micromotors, resulting in the reduction in motion speed, and thus the detection of DNA could be realized *via* the speed change.

Proteins are another group of cancer biomarkers that plays an important role in many biochemical reactions and cell functionalities.[5,86,87,90,100] Yu *et al.* have developed an autonomous micromotor based on gold-nanoparticle-modified self-propelled polyaniline/Pt functionalized with a specific capture antibody and glycidyl methacrylate (GMA) microspheres on the surface for *in situ* detection of cancer biomarkers, carcinoembryonic antigen (CEA) (Fig. 6c).[101] It was observed that the modification of micromotor by antibody led to a decrease in the motion speed under fuel-rich conditions. However, the antibody-functionalized micromotor was able to detect the protein biomarker CEA selectively (Fig. 6d). Since the interaction of antibody and target protein affected the motion speed, the speed change of the micromotor and number of microspheres have been used as analytical signals for cancer biomarker detection. The whole process can be completed within 5 minutes, which can detect the antigen in the concentration range of 1–1000 ng mL^{-1}.[101]

Xu *et al.* reported the detection of circulating tumor cells (CTCs) using NIR-driven fluorescent magnetic nanomotors.[102] They first synthesized the ferro ferric oxide (Fe_3O_4) nanoparticles as the core for magnetic separation after the capture and enrichment of CTCs, and then modified hierarchical silica shell on the surface of Fe_3O_4 nanoparticles to obtain the magnetic hierarchical silica nanoparticles (MHS) (Fig. 6e). Then, platinum (Pt) nanoparticles were generated by *in situ* reduction of chloroplatinic acid and randomly distributed in the shell to obtain the MHS/Pt nanomotor. Under the irradiation of NIR, MHS/Pt nanomotors can be driven by the local thermal gradient resulting from the asymmetric distribution of Pt nanoparticles. Further, for visual detection, they modified fluorescein isothiocyanate (FITC) on MHS/Pt and obtained the fluorescent MHS/Pt/F nanomotor. Finally, the antibody of epithelial cell adhesion molecule (EpCAM) that overexpressed on the surface of CTCs was functionalized onto MHS/Pt/F, which can be used to selectively capture CTCs. They analysed the motion of nanomotors in different environments, optimized the conditions of detecting CTCs and explored the influence of autonomous mixing provided by nanomotors on the capture efficiency of CTCs. Finally, the as-designed nanomotors were used for visual detection of whole blood samples obtained from clinical patients.

Tabrizi *et al.* have demonstrated a new *in vitro* strategy for isolating cancer cells based on the transportability of aptamer-modified nanomotor. In this work, the HL-60 cancer cell was chosen as a model of a target.[103] The thiolated aptamers KH1C12 were immobilized on the surface of gold-based nanomotors *via* self-assemble binding between sulfur (S) and Au atoms. The designed strategy offers superior characteristics of aptamer$_{KH1C12}$/Au$_{nano}$-PEDOT/GC electrode, resulting in high sensitivity, stability, and selectivity for cancer cell detection. Due to the magnetic and catalytic properties of MnO_2–PEI/Ni/Au nanomotor, the oxygen-propelled nanomotor/aptamer can be applied for the isolation of HL-60. The isolated HL-60 was then determined by the aptamer$_{KH1C12}$/Au$_{nano}$PEDOT/GC electrode by the electrochemical impedance spectroscopy technique (EIS) method (Fig. 6f). Upon the addition of HL-60 cancer cells, the charge transfer resistance of aptasensor was significantly increased. The EIS technique revealed that there existed a good linear relationship between peak current with the concentration of HL-60 in the range of 2.5 × 101 to 5 × 105 cells per mL. The experimental detection limit was 250 cells per mL. Thus, the aptamer/Au$_{nano}$-PEDOT/GC electrode has been applied successfully to the determination of HL 60 in human serum.

3.2. Intracellular cancer detection

In the field of nanomedicine, particular attention has been given to intracellular targeting and biosensing, which enables monitoring the cellular functions as well as patient conditions. Since numerous biological processes occur at the subcellular level, the direct and fast internalization of nanomaterial-based probes in the cytosolic space of cells plays a key role in the early detection of cancers and monitoring cell behaviors. Most of the initial research in nanomedicine at the cellular level is focused on the use of different nanoparticles, due to their unique characteristics such as small size, large surface area, and the ability to break through cellular barriers due to enhanced permeation and retention (EPR) effects. The cellular uptake of nanoparticles is governed by different endocytic pathways such as (i) passive delivery, which relies on the intrinsic properties of nanoparticles for their uptake, (ii) facilitated delivery, which involves the functionalization of nanoparticles with specific biomolecules aiding in uptake, and (iii) active delivery, which includes techniques such as microinjection or microporation. Meanwhile, the cellular uptake of nanoparticles facilitates their use for important intracellular applications (Fig. 7a). Intracellular studies have revealed that the mechanism and efficiency of cellular uptake of nanoparticles are primarily being determined by their physicochemical properties (material, size, shape, surface charge and surface functionalization) along with specific cell characteristics and cell density. However, since the interaction of conventional nanoparticle-based probes with cell walls is only based on Brownian motion, the faster movement of these probes can considerably facilitate the internalization process, which in turn, not only increases cell uptake but also improves the sensitivity of the system. Hence, developing micro/

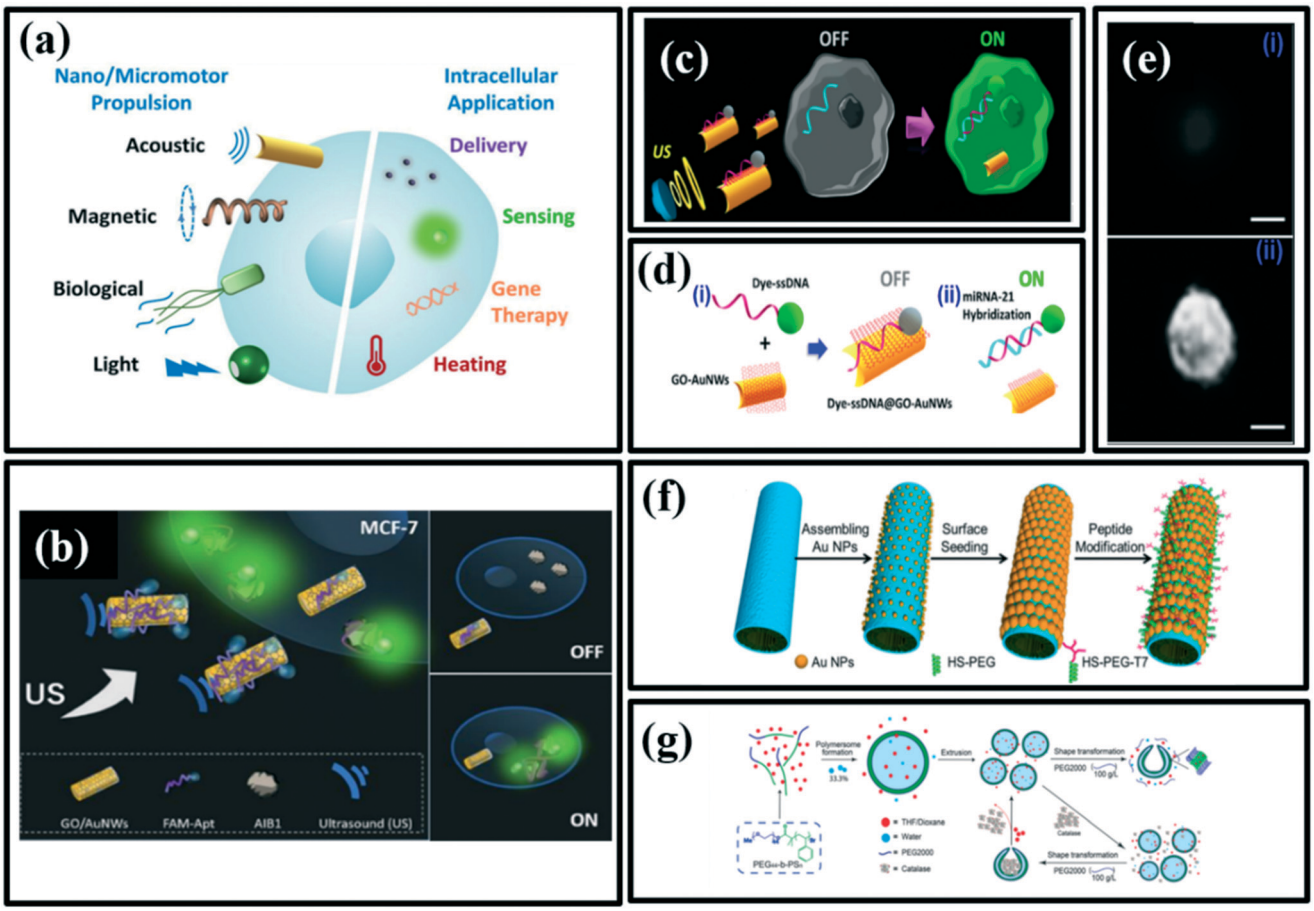

Fig. 7 (a) Nano/micromotors used for a variety of intracellular applications including delivery of therapeutics, sensing of specific target biomolecules, gene therapy, and heating, among others, reproduced with permission from ref. 104, (b) schematic illustration of AIB1 detection in living cancer cells using ultrasound-propelled FAM-AIB1-apt-GO/AuNW motors based on OFF–ON fluorescence switching, intracellular detection of miRNAs by US-propelled ssDNA@GO-functionalized gold nanomotors, reproduced with permission from ref. 106. Schematic illustrations of (c) the "OFF–ON" fluorescent switching system for the specific detection of miRNA-21 in intact cancer cells, and (d) steps involved: (i) immobilization of the dye-ssDNA on the GO-functionalized AuNWs and quenching of the dye fluorescence, and (ii) fluorescence recovery due to the release of the dye-ssDNA from the motor GO-quenching surface upon hybridization with the target miRNA. (e) Fluorescence images of an MCF-7 cell (i) before and (ii) after 20 min incubation with the ssDNA@GO-modified AuNWs under a US field (with 6 V and 2.66 MHz). Scale bar, 10 μm, reproduced with permission from ref. 107 (f) fabrication process of the PtNP-modified polyelectrolyte multilayer microengines coated with a thin AuNS and a tumor-targeted peptide, reproduced with permission from ref. 108, (g) preparation of size-controlled poly(ethylene glycol)-*b*-polystyrene (PEG-PS) stomatocyte-like particles and enzyme-loaded nanomotors, reproduced with permission from ref. 109.

nanomotors for intracellular detection are of great interest and significant progress has been achieved in recent years.[104]

Proteins play an important role in the diagnosis of cancer, as there are a variety of protein biomarkers helping in the detection of the target cancer cells and thus to cure them as well. In particular, the ability to do real-time detection of a protein target in live cells is vital. For example, Geng *et al.*,[105] have designed highly sensitive fluorescent light-up nanoprobes to detect endogenous p53 protein markers and its antagonism in live cancer cells. In one study, Beltrán *et al.* have designed a turn-on fluorescent probe to detect the AlB1 oncoproteins, which plays a key role in the diagnosis of breast cancer cells.[106] In this work, ultrasound-propelled gold nanowire coated with graphene-oxide, functionalized with fluorescein-labeled DNA aptamers was designed as a nanomotor to detect AlB1 oncoproteins in MCF-7 breast cancer cells. In the presence of the target AIB1, the quenched probe (FAM-AIB1-apt) is released from the GO/AuNW surface resulting in the recovery of the fluorescence signal (signal ON), which is shown in Fig. 7b. The ultrasound-driven propulsion of the nanomotors enhanced the fluorescence intensity due to the faster interaction of the nanomotors with the target protein. In addition, this method provided faster penetration of nanomotors into cancer cells and thus, resulted in rapid AlB1 detection within 15 min.[106] Another research group has proposed ultrasound-propelled nanomotor, based on gold nanowires coated with dye-labeled single-stranded DNA/graphene-oxide for the detection of miRNA-21 in intact MCF-7 cancer cells. Once the nanomotor was internalized into the cell, the quenched fluorescence signal (produced by the π–π interaction between GO and a dye-labeled ssDNA) was recovered due to the displacement of

the dye-ssDNA probe from the motor GO-quenching surface upon binding with the target miRNA-21, leading to an intracellular "turn-on" fluorescence switching (Fig. 7c–e). This approach enables fast on-the-move marked detection of the target, even in single cells with a very low content of miRNA-21.[107]

Light-driven micromotors have also been used for developing intracellular biosensors. Particularly, the use of a near-infrared light source is of interest due to its high depth tissue penetration.[104] For example, Wu *et al.* have designed polymer multilayer-based self-propelled micromotors, fabricated with platinum nanoparticles inside, and a thin gold shell outside were functionalized with a mixed layer of a tumor-targeted peptide, and polyethylene glycol to detect HeLa cancer cells.[108] Here, the study showed that the illumination of near-infrared caused a local thermal gradient around the micromotor (Fig. 7f), which accelerated the kinetics of catalytic micromotors at the critical H_2O_2 concentration (0.1%, v/v). These micromotors can be functionalized by targeting ligands for specific cancer detection as well as therapy through the photothermal effect.

Nanoparticles have the advantage of being internalized into the cells. Sun *et al.* have fabricated ultrasmall stomatocyte polymersome nanomotors (USSNs) with the size of around 150 nm using an extrusion method, which could be a promising carriers for biomedical purposes.[109] They demonstrated that the addition of PEG solution to the extruded solution in the presence of enzymes (to power motion *via* chemical gradients) allows for both shape transformation of small polymersomes into stomatocytes, encapsulation of biologics and forms uniform USSNs. Biocatalyst catalase was encapsulated in the inner compartment of the nanomotor, protecting the enzyme while providing enough thrust to propel the motors. The ultrasmall stomatocyte motor system allowed propelled motion by converting H_2O_2 into O_2 in the presence of only 2 mM H_2O_2, and the velocity of motors correlated to the O_2 production. As compared to small stomatocyte nanomotors, ultrasmall stomatocyte motors demonstrate enhanced penetration across the vasculature model and increased uptake by HeLa cells in the presence of fuel. These size-controlled stomatocytes are also reversible, meaning that they can be converted back to polymersomes by adding an organic solvent (Fig. 7g).

4. Cancer cells imaging

The prompt and timely diagnosis of the disease is the most important stage in eradicating the disease completely. In addition to identifying cancer cells and biomarkers, it is also possible to diagnose tumors through tissue imaging. In particular, micro/nanomotors can significantly speed up the imaging process owing to their motions and fast positioning inside the target tissue.[114–116] Today, the potential applications of the micro/nanomotors in various imaging techniques, including fluorescent imaging (FI),[117,118] magnetic resonance imaging (MRI),[119,120] computed tomography (CT)[121] have been investigated. Among them, MRI and optical fluorescence imaging are the most applicable techniques due to their simplicity and noninvasiveness.[122] In this section, we discuss the latest research done in the field of cancer cell imaging by means of micro/nanomotors.

Magnetic resonance imaging (MRI) is a powerful technique being widely used in clinical applications. In the field of micro-/nanomotors, the magnetic field is a promising fuel-free power source due to its noninvasiveness and high penetrability. Generally, by incorporating magnetic components, micro-/nanomotors can exhibit effective controllability and navigation under the external magnetic field. It should be noted that the mobility of micro-/nanomotors generally relies on a low-strength magnetic field, which is biocompatible and harmless to organisms.[123] Benoit *et al.* have used a hybrid magnetotactic micromotor to perform MRI for the visualization of implanted tumors in mice.[124] This study has exhibited that AMB-1 bacteria with small magnetite particles generate T1-weighted positive contrast, subsequently, enhance the *in vivo* visualization by magnetic resonance imaging. Following intravascular injection of copper (Cu)-labeled AMB-1, positron emission tomography imaging revealed increasing colonization of tumors and decreasing infection of organs after 4 hours. This investigation further found that the Magnetospirillum magneticum AMB-1 could colonize mouse tumor xenografts and produce positive MRI contrast could potentially provide a useful tool for improving MRI visualization to track cancer in preclinical and translational studies.

In another work, Wu *et al.* have proposed red blood cell (RBC)-based micromotors for both cancer imaging and therapeutic applications.[125] These RBC-based micromotors consist of three imaging agents (hydrophilic CdTe quantum dots, QD) with great stability against photo bleaching, anti-cancer drug doxorubicin (DOX), which also provides a visualization of their loading inside the RBC motors through the self-fluorescent emission. In addition, the third component of the motors is magnetic nanoparticles (MNPs), which are applied not only for the propulsion of motors under the ultrasound field but also used for magnetic resonance (MR) imaging (Fig. 8a). The simultaneous encapsulation of these three components thus permits controlled navigation, imaging, and drug delivery, which enables the multi-cargo-loaded RBC micromotors to serve as a potential mobile theranostic tool.

Fluorescent imaging (FI) has been widely used in the field of biomedicine, such as for the examination of cells and tissues, the localization of micro/nanocarriers. The fluorescence imaging technology, especially with the use of multifunctional nanoparticles has many advantages for different applications in biomedicine, such as live-cell tracking, drug screening, image-guided therapy, blood cell counting, *etc.*[126–136] Furthermore, this noninvasive imaging

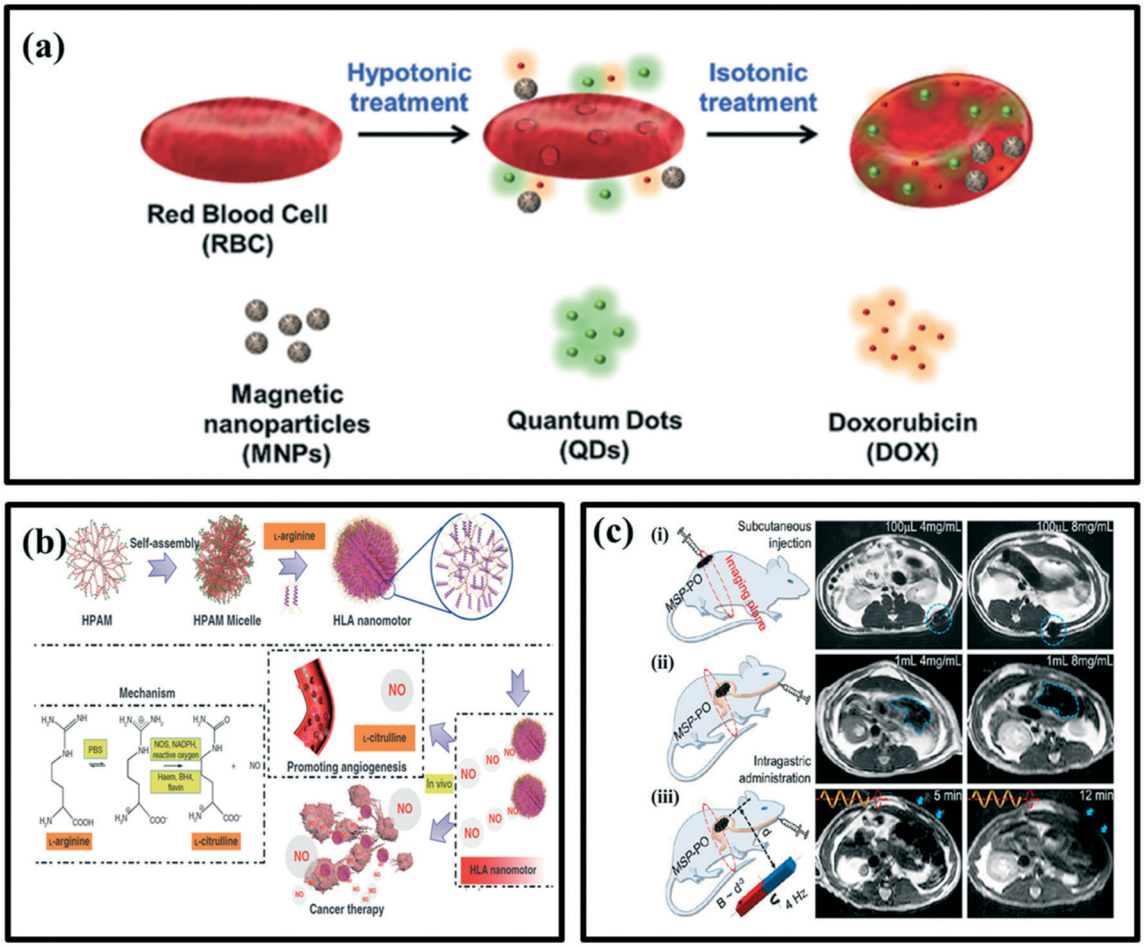

Fig. 8 (a) Schematic preparation of multicargo-loaded RBC micromotors towards theranostic applications. RBC cells are concurrently loaded with QDs imaging nanocrystals, anti-cancer drug doxorubicin (DOX), and magnetic Fe_3O_4 nanoparticles through a hypotonic dilution-based encapsulation method, reproduced with permission from ref. 125, (b) schematic illustration of the formation of zwitterion-based nanomotor and NO generation principle, reproduced with permission from ref. 138 (c) (i) MSP swarm of two different concentrations inside the subcutaneous tissues. (ii) MSP swarm of two different concentrations inside the stomachs. (iii) MSP swarm with the same concentration but subject to actuation and steering (with a rotating magnetic field) of different time periods before MR imaging across the rat's stomach, reproduced with permission from ref. 117.

technology would not cause any harmful ionization effects on the cells and tissues. This technology also shows advantages such as low cost, high sensitivity, multicolor imaging, and simple operation. Benefiting from the synergy of imaging and motion, the resultant micro/nanomotors not only can be tracked in real-time *in vitro* and even *in vivo* but also used to realize targeted delivery/therapy in a destinated location with vision-based control. There are mainly two ways to endow micro/nanomotors (MNMs) with fluorescent properties. One way is through surface modification of the probes, and another is using auto fluorescent materials as the building elements.[137] Wan *et al.* reported a nitric oxide (NO)-driven nanomotor made up of hyperbranched polyamide/L-arginine (HLA) based on endogenous biochemical reactions in the human body involving the conversion of amino acid L-arginine to nitric oxide by NO synthase (NOS) or reactive oxygen species (ROS) (Fig. 8b).[138] The ROS *in vivo* were simulated with H_2O_2, and the kinetic behavior of nanomotors was studied *in vitro*. The proposed HLA system uses L-arginine as fuel and the produced NO provides the driving force plus some additional benefits such as promoting endothelialisation, anticancer effects and fluorescent self-imaging of nanomotors. A good fluorescent property of hyperbranched polyamide (HPAM) facilitates the self-imaging of the nanomotors in cellular conditions, which further increases the possibility of tracking the devices *in vivo* in the future.

In another study, Yan *et al.* have reported the fabrication of biohybrid magnetite robots from spirulina microalgae *via* a dip-coating process in Fe_3O_4 suspensions. The microrobots have been featured with the superparamagnetic properties, the desired structure and fluorescence inherited from biological matrix.[117] The strong red light emission from the microrobots could be easily observed upon the green light illumination without adding any fluorescent markers, which can be utilized for *in vivo* bioimaging and remote biomedical diagnostic. As shown in Fig. 8c, the *in vivo* magnetic resonance imaging has been used to track a swarm of

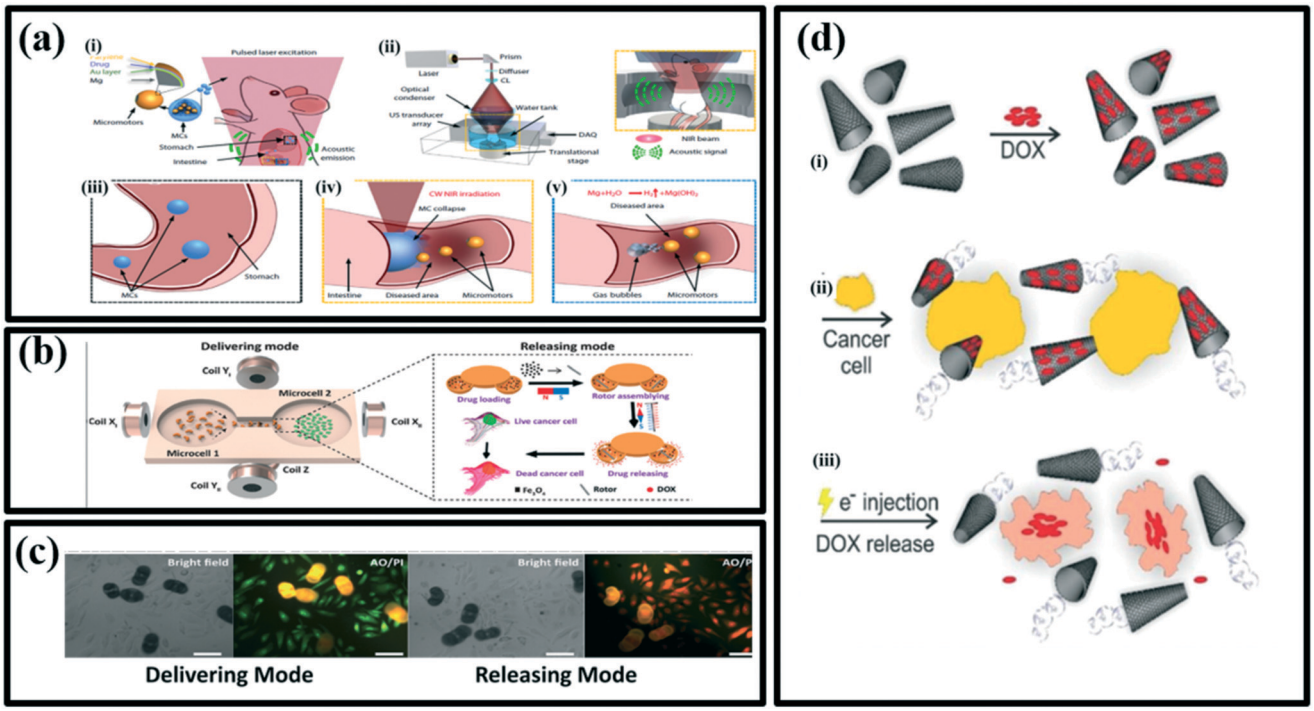

Fig. 9 (a) (i) Schematic illustration of PACT-guided microrobotic system *in vivo*, (ii) schematic illustration of PACT in the GI tract. Inset shows the confocal design of light delivery and PA detection where US: ultrasound; C:, conical lens; DAQ: data acquisition system, (iii) enteric coating prevents the decomposition of MCs in the stomach, (iv) external continuous-wave NIR irradiation-induced collapse of the MCs on-demand in the targeted areas, (v) active propulsion of the micromotors promoted retention and cargo delivery efficiency in intestines, reproduced with permission from ref. 121, (b) schematic illustrations of PPBMs describing the delivering and releasing mode, respectively, reproduced with permission from ref. 140 (c) bright field and fluorescent images of HeLa cells incubated with DOX-loaded pine pollen-based micromotors. Stained with acridine orange (AO) and propidium iodide (PI) showing the dead cells (red fluorescence with acridine orange staining) and live cells (green fluorescence with propidium iodide staining). Scale bars, 50 μm, reproduced with permission from ref. 140, (d) an overview of the loading/release of doxorubicin on/from the n-rGO/Pt micromachines, (i) physical adsorption of doxorubicin on the outer layer of micromachine (n-rGO), (ii) bubble-propelled swimming of micromachines loaded with doxorubicin in the presence of cancer cells (yellow), (iii) the release of doxorubicin upon applying an electrical potential and delivering the drugs to cancer cells, reproduced with permission from ref. 141.

microrobots inside rats' stomachs, which is a 'deep' organ where fluorescence-based imaging ceased to work because of its penetration limitation. Meanwhile, the microswimmers were able to degrade and exhibit selective cytotoxicity towards the cancer cell lines, subject to the thickness of the Fe_3O_4 coating, which could be tailored *via* the dip-coating process. To conclude, the microrobots have been successfully propelled inside the rat's stomach using a rotating magnetic field and noninvasively tracked through cross-sectional MR imaging.

Photoacoustic (PA) computed tomography (PACT) is a noninvasive hybrid imaging technique that combines optical excitation and acoustic detection to realize high contrast, high resolution, and deep penetration in biological tissues.[139] Wu *et al.* have reported a PACT-guided microrobotic system (PAMR), with the controlled propulsion and prolonged cargo retention *in vivo*.[121] The enveloped micromotors in microcapsules were stable in the stomach and exhibited efficient propulsion in various biofluids once released. The micromotor capsules (MCs) were administered to the mouse (Fig. 9a(i)). NIR illumination facilitates the real-time PA imaging of MCs and subsequently triggers the propulsion of the micromotors in targeted areas of the GI tract. NIR illumination onto the mouse-generated PA signals, which were subsequently received by the transducer array (Fig. 9a(ii)). Ingestible Mg-based micromotors were encapsulated in the enteric protective capsules to prevent reactions in gastric acid and allow direct visualization by PACT (Fig. 9a(iii)). PACT monitored the migration of MCs through the intestines in real-time while continuous-wave (CW) near-infrared (NIR) light irradiation-induced phase transition of microcapsules and triggered the propulsion of the micromotors (Fig. 9a(iv)). In addition, NIR irradiation helps to disintegrate the capsules to release the cargo-loaded micromotors. This autonomous and efficient propulsion of the micromotors enhanced the retention of cargo carriers (*i.e.*, micromotors) in targeted areas of the GI tract (Fig. 9a(v)). Furthermore, to investigate the cargo release kinetics of the micromotors, researchers have encapsulated a fluorescent anticancer drug (DOX) into the alginate layer of the micromotors. The release of DOX from the micromotors was characterized using a UV-visible spectrophotometer.

Inspired by nature and renewable materials, Sun *et al.* have developed pine pollen-based micromotors (PPBMs) for

targeted drug release, with excellent maneuverability in multiple media, efficient drug encapsulation and on-demand release to treat HeLa cancer cells.[140] These versatile biohybrid micromotors were synthesized by simultaneous encapsulation of the magnetic particles and drug (DOX) into two hollow air sacs of pine pollen *via* vacuum loading. The resultant PPBMs perfectly inherit the intrinsic functionalities of pine pollen, not only capable of maintaining a stable morphology in various extreme environments to protect the drug from damage, but also allowing *in vivo* fluorescence imaging without any surface modification. Under different input magnetic fields, the encapsulated magnetic Fe_3O_4 endows individual PPBMs with three motion modes (*i.e.*, rolling, tumbling and spinning) and the capability for controllable navigated locomotion. Furthermore, these PPBM individuals can form a dynamic swarm by regulating the input magnetic field. Swarm PPBMs also show controllable and continuous locomotion trajectories in the complex biological fluids, even on biological tissues (mouse small intestine). Besides displaying controlled propulsion, these biohybrid micromotors also exhibit a specific mechanism to release the therapeutic drug on demand using a field generated by the rotating magnetic block. To demonstrate the ability of transportation of the drug *via* PPBMs, a custom-made cell culture dish of two microcells was developed. These two cells were used to keep PPBMs and HeLa cancer cells separately. By applying the magnetic field, the entire process of delivering and releasing the loaded drug has been carried out successfully as shown in Fig. 9b.[140] For the delivering mode, a rotating magnetic field has been used. However, DOX-loaded PPBMs have shown therapeutic effects in both, delivering and releasing modes. In the releasing mode, 40% of the cells were killed as compared to that of 15% occurred while operating in the delivering mode (Fig. 9c).

Khezri *et al.* have demonstrated the capability of a powerful bubble-propelled micromachine based on reduced nanographene oxide for drug delivery. n-rGO/Pt micromachines showed fast speed at very low concentrations of hydrogen peroxide.[141] The loading efficiency of the micromachines by DOX molecules was also very high, which indicates a successful loading mechanism based on a simple π–π interaction (Fig. 9d(i)). The force applied by the bubble propelled the micromachines towards the cancer cells (Fig. 9d(ii)). This research group has introduced a new on-demand drug-release mechanism based on an electrochemical stimulus. It was shown that electron injection into DOX@n-rGO/Pt micromachines leads to expulsion of DOX from the micromachines in motion in a very short time (Fig. 9d(iii)). To elucidate the mechanism of the therapeutic effect of DOX@n-rGO/Pt micromachines, living cells fluorescence imaging of T47D was carried out.

5. Cancer treatment

Although worldwide efforts to develop efficacious cancer treatment with low side effects, cancer is still considered one of the most threatening diseases to mankind and a significant challenge for medical researchers. Although a wide variety of approaches have been devoted to clinical cancer treatment, such as radiotherapy, phototherapy, chemotherapy and gene therapy, it is still hard to rely completely on these techniques. Utilizing nanomaterials can improve the efficacy of current methods as well as reduce the side effects. In particular, micro/nanomotors have demonstrated considerable promise for cancer therapy due to their efficient characteristics, which make them exceptional among new and innovative nanomaterials proposed for cancer treatment *via* nanomedicine. The faster interaction of micro/nanomotors results in higher cellular uptake and therefore, the enhancement of drug delivery to tumor sites can be achieved. This can ultimately enhance the efficiency of cancer therapy by several folds. Here we review the recent progress of micro/nanomotors in cancer treatments including chemotherapy and phototherapy (Table 2).[142–144]

5.1. Chemotherapy

Conventional chemotherapy is still one of the most common approaches for the treatment of most types of cancers.

Table 2 The recent advanced applications of micro/nanomotors in drug delivery

Micro/nanomotor	Propulsion fuel/mechanism	Chemotactic agent	Target	Ref.
BMV–CCMV@Pt Janus virus nanomotors	Catalytic/H_2O_2	Tamoxifen	MDA-MB-231 breast cancer cell	152
As–Pt Janus nanomachines	Catalytic/H_2O_2	DOX	A549 cells	150
PASP/Fe–Zn microrockets	Gastric acid/H_2 bubbles	DOX	Gastric cancer cells	147
Iron oxide MNC@Au@PDA/PEG/FA nanorobots	Magnetic force	DOX	Hep3b cell lines	153
Spermbots/Fe–Ti	Magnetic field	DOX-HCl	3D cervical and ovarian cancer cell cultures	149
MIL-8-ICG@ZIF-8 nanomotors	NIR-driven	DOX	4T1 cells	154
mC@SiO2 nanomotors	NIR-driven/thermal gradient	DOX	MCF-7 breast cancer cell	155
Mg-PLGA micromotors	Mg–water reaction/H_2 bubbles	H_2 and DOX	4T1 tumor cells	151

Abbreviations: BMV: Brome mosaic virus, CCMV: cowpea chlorotic mottle virus, PASP: poly(aspartic acid), MNC: magnetic nanoclusters, PDA: polydopamine, FA: folic acid, ICG: indocyanine green, PLGA: poly(lactic-co-glycolic acid).

However, unfavourable side effects to patients, lack of tumor selectivity and unsatisfied delivery efficiency of the chemotherapy method hinder the treatment of cancer. In the last decade, many efforts have been devoted to the development of nano carrier-based drug delivery systems in a quest to improve the therapeutic efficacy of chemotherapy while reducing systemic toxicity. In these attempts of improvement in the current chemotherapy, nanomotors have also come into the picture as an advanced asset in the amelioration of therapy. As the interaction between the nanocarriers and the target cancerous tissue is absolutely based upon the Brownian motion of the nanoparticles, it is expected that the self-propelled micro/nanomotors would have a stronger interaction with the cell wall. This can lead to higher cellular uptake in a shorter time by using micro/nanomotor-based nanocarriers.[145,146] Zhou *et al.* have demonstrated that poly(amino-acid)-based microdevices can be used for targeted anticancer drug delivery *in vivo*.[147] The micromachines consisted of poly(aspartic acid) (PASP) microtube, a thin Fe intermediate layer, and a core of Zn (Fig. 10a). The motor's zinc core reacts with the gastric acid fluid and uses it as a fuel to generate a propulsion force associated with the proton depletion reaction and thus hydrogen bubbles production occurs. The chemotherapy medication doxorubicin (DOX), used to treat cancer, is bonded onto the PASP surface and the microrocket can magnetically locate the targets, be trapped in the gastric mucus gel layer, and slowly release concentrated DOX payloads onto the stomach wall in an acidic environment. All materials in microrockets are biocompatible and biodegradable and can be readily decomposed by gastric acid or by proteases in the digestive tract. In particular, PASP/Fe–Zn microrockets can serve as microcarriers *via* various intermolecular interactions for diverse bio applications *in vitro* and *in vivo*.

Spermbots are biocompatible hybrid machines that are propelled by single spermatozoa and have promising features for powering nano and microdevices.[148] Xu *et al.* have successfully loaded human sperm with a chemotherapeutic drug doxorubicin hydrochloride (DOX-HCl) and perform the treatment of relevant 3D cervical cancer and patient-representative 3D ovarian cancer cell cultures.[149] They showed that human sperm can encapsulate DOX-HCl in their crystalline nuclei and that hydrophilic drugs encapsulated by the sperm are well protected from dilution by the body fluids and enzymatic degradation due to the compact membranes of sperm. The presence of chromosomes in the sperm head has the potential to provide ample opportunities for intracellular storage of DNA-binding drugs such as DOX-HCl. In addition, the ability to self-propel combined with peristalsis of female reproductive organs makes sperm attractive for carrying drugs for long durations and distances inside the gynecological tract in a protected manner. Inset shows an alternative design for carrying multiple drug-loaded sperm for future drug dose control.[149]

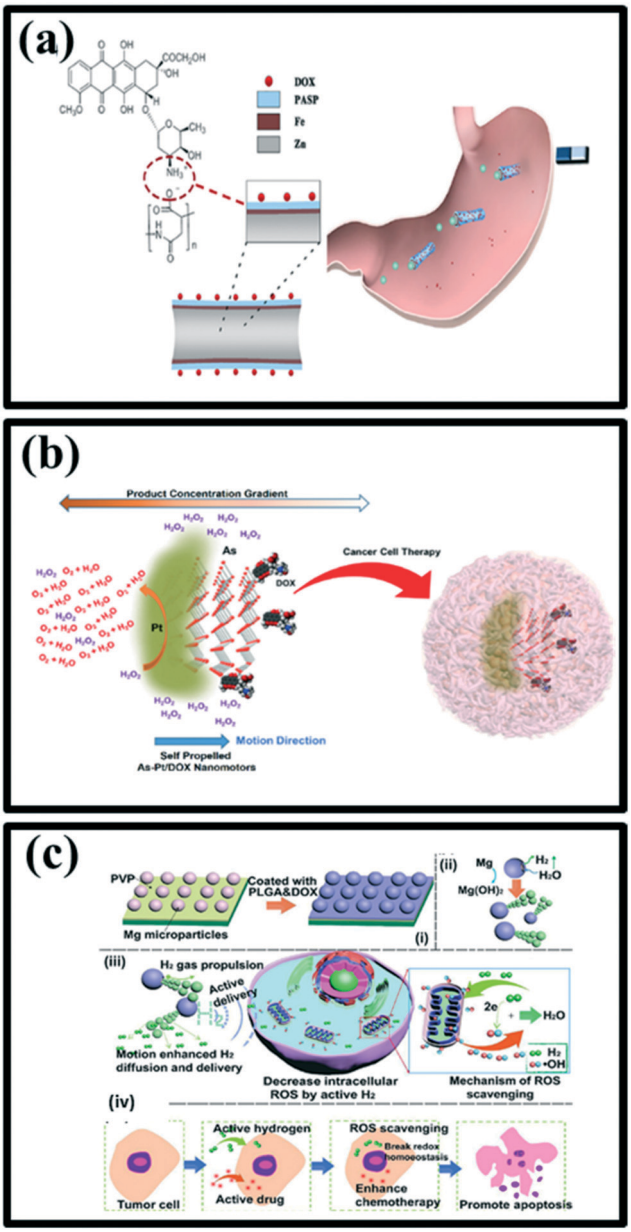

Fig. 10 (a) Schematic structure of a DOX/PASP/Fe–Zn MR (b) and its application for effective localization in the stomach, reproduced with permission from ref. 147, (b) self-propelled Janus As–Pt/DOX nanomotors and their application as an anticancer drug carrier, reproduced with permission from ref. 150 (c) schematic illustration of (i) Mg-based micromotors, (ii) propulsion mechanism of Mg micromotors, (iii) Mg-based micromotors as hydrogen generator and drug delivery platform for locally active H_2 generation to scavenge OH, (iv) enhanced active hydrogen chemotherapy of Mg micromotors, reproduced with permission from ref. 151.

Rosli *et al.* have explored arsenene nanoparticles modified with platinum to form Janus As–Pt nanomotors. Firstly, propulsion capabilities were studied and their results demonstrated fast circular propulsion of As–Pt nanomotors, with H_2O_2 as fuel, by self-diffusiophoresis.[150] Interestingly, at a significantly low concentration of H_2O_2 (0.25%), these As–Pt nanomotors could still successfully move with a speed of 3

μm s^{-1}. Following that, the biocompatibility and drug loading competency of these As–Pt nanomotors were investigated. As–Pt nanomotors were found to be fast, nontoxic at a low concentration, possess high cellular uptake into A549 cells and have promising drug loading capabilities of doxorubicin (DOX) (Fig. 10b).

Liu *et al.* have designed a biodegradable self-propelled hybrid Mg-based micromotor for the enhancement of active and synergistic hydrogen chemotherapy (Fig. 10c(i)).[151] Biodegradable micromotors were fabricated by using Mg microparticles as templates, subsequently coated with poly (lactic-co-glycolic acid) (PLGA) asymmetrically, which is promising for drug delivery due to its degradable characteristics and improved drug loading capacity. The small opening of the Mg-motor could act as an Mg–water reaction interface for H_2 generation under the gastric and intestinal fluid or even serum environment. Therefore, resulting in autonomous motion (Fig. 10c(ii)). H_2 produced by Mg–water reaction was able to achieve the enhanced diffusion due to the motion of micromotors, offer the possibility of enhanced reactive oxygen species (ROS) scavenging (special for $^{\bullet}OH$) (Fig. 10c(iii)). By using Mg micromotors for active and synergistic hydrogen chemotherapy, an outstanding performance towards tumor cells was achieved (Fig. 10c(iv)). The local hydrogen generation and active motion capabilities provide a great promise for hydrogen chemotherapy, and the doxorubicin loading on micromotors improves the chemotherapy efficacy for 4T1 tumor cells with a concentration as low as 100 μg Ml^{-1}.

5.2. Phototherapy

Traditional cancer treatment includes surgery, chemotherapy and radiotherapy. However, complete eradication of tumors is quite difficult. On the other hand, chemotherapy and radiotherapy can produce severe side effects on healthy cells. Therefore, in order to overcome these shortcomings of current treatment and achieve desirable and satisfactory treatment results, it is necessary to use a more effective yet non-invasive treatment methods. To date, various treatment strategies such as photodynamic therapy (PDT), photothermal therapy (PTT), gene therapy and immunotherapy have been developed as effective methods to improve treatment outcomes. Among them, phototherapies, including PDT and PTT, have attracted widespread attention in recent years due to their high efficiency, noninvasive light conversion, excellent tumor targeting, and minimal side effects. Most importantly, the rapid development of nanotechnology and nanomaterials has greatly enhanced the advancement of phototherapy in the eradication of various types of cancer.[126,130,136,156] The use of micro/nanomotors is a very effective way to develop and advance the treatment of cancer with the help of phototherapy. In this section, we discuss the application of micro/nanomotors in both photothermal therapy and photodynamic therapy.[157–160]

5.2.1 Photothermal therapy. Photothermal therapy (PTT) is a cancer treatment that kills cancer cells by the heat generated in tumor tissue that is exposed to near-infrared (NIR) light through which the NIR adsorbents facilitate heat generation. Choi *et al.* have developed a NIR light-triggered nanomotor system for active photothermal cancer therapy using PEG_{44}-*b*-PS_{141} copolymers. They prepared PEG_{44}-*b*-PS_{141} nanomotors encapsulating Cu(II) 5,9,14,18,23,27,32,36-octabutoxy-2,3 naphthalocyanine (NC) and Pt nanoparticles (NPs). Cu(II) 5,9,14,18,23,27,32,36-octabutoxy-2,3 naphthalocyanine can be used as a strong NIR light absorber, while Pt NPs as an engine and catalytic decomposer of H_2O_2 (Fig. 11a).[161] The NIR light illumination could trigger temperature-responsive behaviours of stomatocyte nanomotors. In addition, the nanomotors autonomously moved toward H_2O_2 released from cancer cells by chemotaxis and showed the photothermal ablation effect on cancer cells under NIR light illumination, demonstrating the feasibility for photothermal cancer therapy (Fig. 11b).[161]

Shao *et al.* have designed a photothermally driven biodegradable nanomotor (PNM), based on hemispherical gold-coated poly(ethylene glycol)benzoic-imine-poly(*d*,*l*-lactide) (PEG-PDLLA) polymersomes Fig. 11c. Upon irradiation with NIR light, these nanomotors undergo autonomous motion as a function of the laser power. Such nanomotors were able to traverse through the biological membranes and effectively penetrate HeLa tumor tissues, hence permit the active transportation of molecular and macromolecular cargo either by encapsulation or co-delivery. This offers opportunities for their applications in deep tissue penetration and drug delivery. Furthermore, the ability of PNMs to be loaded with functional components that can be released intracellularly can permit enzymatic catalysis to take place in living cells.[162]

Xuan *et al.* have designed NIR light-powered Janus mesoporous silica nanomotor (JMSNM) with the macrophage cell membrane (MPCM) cloaking that can actively seek cancer cells and thermomechanically percolate through the cell membrane (Fig. 11d). Upon exposure to NIR light, a heat gradient across the Janus boundary of the JMSNMs is generated by the photothermal effect of the Au half-shells, resulting in a self-thermophoretic force that propels the asymmetric structure of MPCM@JMSNMs to overcome the Brownian motion and achieve a directional motion. In a biological medium, the MPCM camouflaging not only can prevent dissociative biological blocks from adhering to JMSNMs, but also improves the targeting ability of the nanomotors to recognize specific cancer cells. The bioinspired propulsion mechanism and recognition capability enable JMSNMs to achieve active targeting and binding to the membrane of cancer cells. The subsequent illumination of NIR light then triggers the photothermal effect of MPCM@JMSNMs to thermomechanically perforate the cytomembranes for guest molecular injection (Fig. 11d(i–iv)). This group has successfully demonstrated that both the functionalized gold half-nanoshell JMSNMs and natural MPCMs can be engineered to actively bind the cancer cells

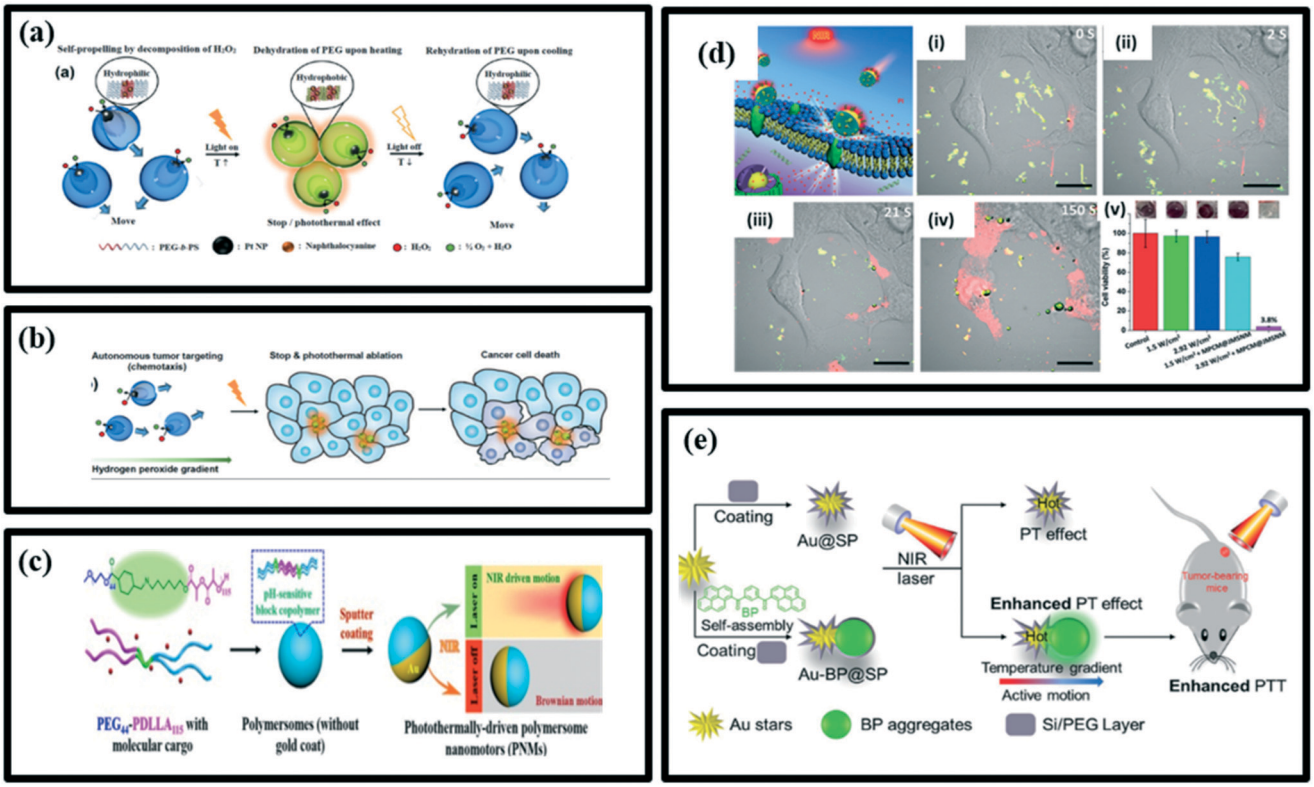

Fig. 11 (a) Schematic representation of a light-guided nanomotor system using PEG44b-PS141/naphthalocyanine (NC) and Pt nanoparticles (Pt NPs) powered by the conversion of hydrogen peroxide (H_2O_2), reproduced with permission from ref. 161, (b) schematic illustration for the autonomous photothermal ablation of cancer cells using the nanomotors, reproduced with permission from ref. 161, (c) design strategy of PNMs and photothermomechanically perforating the cancer cell membranes activated by NIR light, reproduced with permission from ref. 162, (d) schematic illustration of MPCM@JMSNMs applied to thermomechanically percolating the cell membranes. (i–iv) Time-lapse CLSM images of MPCM@JMSNMs-embedded 4T1 cancer cells upon illumination with 2.92 W cm^{-2} NIR light. Scale bars = 20 μm. (v) Evaluation of the therapeutic efficacy in each group, measured by MTT assay, reproduced with permission from ref. 163. (e) Schematic illustration of a selfpropulsion AuBP@SP Janus nanoparticle for cancer cell treatment under NIR laser irradiation, reproduced with permission from ref. 165.

and perform targeted photothermal cancer therapy *in vitro* (Fig. 11d(v)).[163]

Gold nanoparticles (AuNPs) are being widely used for photothermal treatment (PTT) due to their photothermal effect (PT) as AuNPs can transfer heat to their surroundings and increase the temperature of the region through electron–photon inertia under the influence of light radiation.[164] Yang *et al.* have prepared the structure-controllable Janus-like nanohybrids named Au-BP@SP, in which the internal heterojunction, composed of inorganic gold stars and organic bis-pyrene nanoaggregates, was coated with PEGylated silica shell. The Au-BP@SP nanohybrids showed thermophosis with active motion and enhanced PT effect under NIR irradiation. As a result, Au-BP@SP nanohybrids showed significantly improved photothermal tumor therapeutic outcomes compared with conventional gold nanoparticles (Au@SP) themselves. The Au-BP@SP Janus nanohybrids processed active motion driven by the temperature gradient between the two sides of nanohybrids under NIR irradiation. The stronger PT effect of Au-BP@SP Janus nanohybrids could be attributed to the effective conversion of kinetic energy into heat by the collisions, which consequently increases environmental temperatures. As a result, the Janus Au-BP@SP nanohybrids have enhanced PTT *in vitro* and *in vivo* for cancer therapy (Fig. 11e).[165]

5.2.2 Photodynamic therapy. Photodynamic therapy (PDT) is a minimally invasive, clinically approved treatment that can exert selective cytotoxic activity typically on malignant cells. Photodynamic therapy (PDT) utilizes a photosensitizer (PS), light and O_2 to produce cytotoxic reactive oxygen species (ROS) that kill the cancer cells by oxidizing biomolecules. This method involves the application of a light-sensitive material followed by wavelength irradiation of a synthesizer absorption band.[166,167] Recently, effective nanomaterials-based photosensitizers (some with enhanced fluorescence brightness) have successfully been developed to greatly improve the singlet oxygen generation efficiency and thus PDT treatment efficacy.[126,127,129,130,132,135,136,156] It can also benefit from the combination of micro/nanomotors due to their unique contributions as mentioned above. In this review, we will discuss a few successful examples of applying micro/nanomotors in cancer photodynamic therapy.

Gao *et al.*[168] have proposed red blood cell-mimicking (RBCM) micromotors capable of actively delivering oxygen

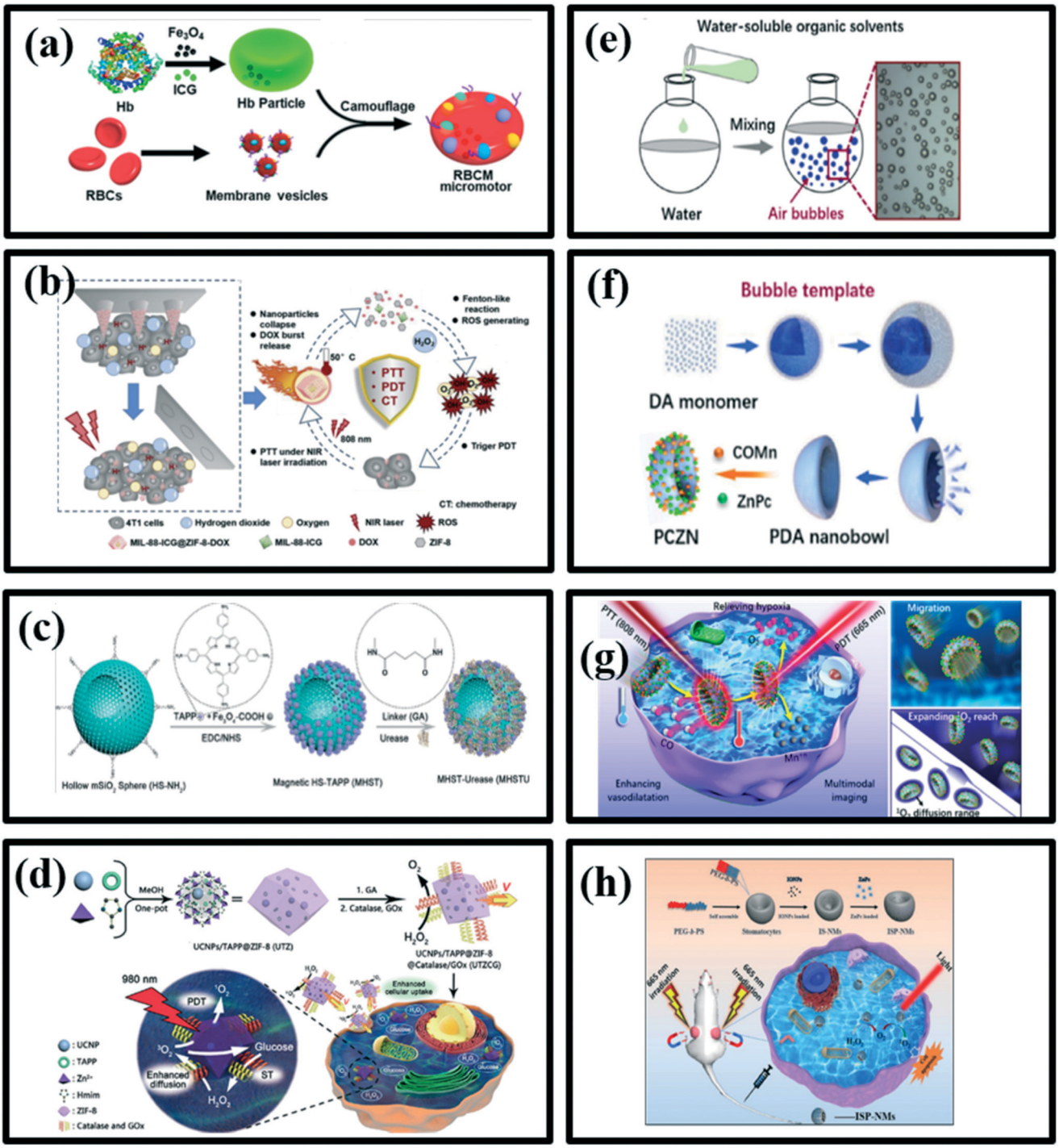

Fig. 12 (a) Schematic fabrication procedure of RBCM micromotors, reproduced with permission from ref. 168, (b) schematic illustration of MIL-88-ICG@ZIF-8-DOX nanoparticles for synergistic photothermal/photodynamic/chemotherapy of tumor, reproduced with permission from ref. 169, (c) schematic illustration of the fabrication of urea-propelled magnetic micromotors (MHSTU), reproduced with permission from ref. 170, (d) schematic illustration showing the fabrication process of a UTZCG nanomotor and synergetic photodynamic-starvation therapy by self-accelerated cascade reactions, reproduced with permission from ref. 171, (e) schematic diagram of air outgassing in the form of bubbles after mixing water and water-soluble organic solvent, reproduced with permission from ref. 172. (f) DA polymerization using bubbles as a template to form PDA nanobowls and PCZNs fabrication,[172] (g) PCZNs synergistic anticancer mechanism and its multiple functions, reproduced with permission from ref. 172, (h) schematic diagram of magnetic field-assistant tumor targeting of ISP-NMs and their O_2 generation, movement and PDT process for cancer treatment, reproduced with permission from ref. 173.

and photosensitizers, indocyanine (ICG), to the tumor for effective PDT (Fig. 12a). These micromotors were fabricated by coating RBC-shaped hemoglobin particles that encapsulated Fe_3O_4 nanoparticles and ICG with RBC

membranes. Due to the biconcave discoidal structures and the presence of Fe_3O_4 nanoparticles, the micromotors could be powered by an acoustic field and navigated towards the tumor site with magnetic guidance in the blood. Higher oxygen affinity of haemoglobin ensured the micromotors to carry sufficient oxygen to cancer cells. Meanwhile, the RBC membrane-camouflaging protected the micromotors from biofouling and immune clearance, which facilitated their motion in whole blood. These characteristics together led to the enhancement of PDT efficiency.[168]

Wu *et al.*[169] have constructed a core–shell dual metal–organic framework (MOFs) using MIL-88 as internal core and ZIF-8 as an external shell, which was expected to be employed as a versatile nanoplatform for synergistic photothermal/photodynamic/chemotherapy of tumor (Fig. 12b). In this work, an indocyanine green (ICG) photosensitizer was encapsulated into internal MIL-88 by the impregnation method. The MIL-88 was expected to improve further ICG stability, avoiding rapid aggregation and photo-degradation due to the breathing behaviour. Finally, DOX was loaded into the ZIF-8 shell. After irradiation, the ICG could convert the light energy into heat or ROS to kill tumor cells. The site- and time-specific controlled drug release profile could be realized since the degradation of ZIF-8 could be triggered by the acidic tumor microenvironment and the high temperature-induced by PTT. Additionally, MIL-88 functioned as an intrinsic oxygen producer *via* a Fenton-like reaction, generating continuous oxygen to strengthen the PDT efficacy. This multifunctional core–shell dual MOFs based on MIL-88 and ZIF-8 not only served as a drug loading platform with two separate delivery zones but also a releasing switch and self-stimulated oxygen producer.[169]

Xu *et al.*[170] have developed an enzymatic magnetic hollow mesoporous SiO_2 micromotor loaded with 5,10,15,20-tetrakis(4aminophenyl)porphyrin (TAPP, a highly efficient but hydrophobic photosensitizer) (MHSTU), as a mobile photosensitizer platform (Fig. 12c). TAPP was loaded onto the magnetic nanoparticles, which were anchored on the external surfaces of the hollow mSiO_2 microspheres. Due to chemical bonding between carboxylic groups of magnetic nanoparticles (Fe_3O_4–COOH) and amine groups of TAPP, TAPP molecules were separated in a monomeric state to avoid the quenching of PDT effect caused by self-aggregation in the physiological conditions. The as-prepared hollow microspheres formed by a one-step reaction in bulk synthesis have intrinsic asymmetric property contributed by the holes on the surfaces of the hollow mSiO_2 spheres (HS). MHSTU can be propelled by the urease-triggered biocatalytic reaction of urea on its asymmetric structure. The motors also possess magnetotaxis behaviour for remotely targeted transportation by the external magnetic field. The random motion of the urea-driven MHSTU can increase the O_2 generation rate by improving the accessibility to O_2 molecules and spread toxic O_2 molecules to a much larger area, resulting in enhanced photodynamic toxicity. They have demonstrated the antibacterial PDT process over gram-negative bacteria, *Escherichia coli* (*E. coli*) *via* flow cytometry assay and fluorescence microscopy.[170]

Enzyme-driven micro/nano-motors have been emerged as a promising self-propelled therapeutic nanosystem owing to good biocompatibility, noninvasiveness, and fuel bioavailability. You *et al.*[171] have presented self-propelled enzyme-modified zeolitic imidazolate framework-8 (ZIF-8, a kind of metal–organic framework (MOF)) encapsulating up-conversion nanoparticles (UCNPs) and hydrophobic photosensitizers (PSs), as an enzyme-driven nanomotor with synergetic therapeutic capabilities of both near-infrared (NIR)-responsive PDT and biocatalytic reaction-activated starvation therapy. As illustrated in (Fig. 12d), ZIF-8 is coated onto the as-prepared UCNPs to obtain a core–shell structure, and the porous shell of ZIF-8 serves as a nanocarrier to load 5,10,15,20-tetrakis(4-aminophenyl)porphyrin (TAPP, a typical water-insoluble photosensitizer), denoted as UCNPs/TAPP@ZIF-8 (UTZ). UCNPs, as the core of the nanomotor, are capable of upconverting NIR light into a blue light that is absorbed by TAPP to generate cytotoxic O_2 for efficient PDT. Two enzymes, catalase and GO*x*, were modified onto the surface of ZIF-8 by utilizing glutaraldehyde (GA) as linker molecules to obtain the therapeutic nanomotors, named as UCNPs/TAPP@ZIF-8@catalase/GO*x* (UTZCG). The oxidative decomposition of glucose catalyzed by GO*x*, on the other hand, consumes glucose to cut off the glucose metabolism of cancer cells for ST, as time produces H_2O_2 around nanomotors. Then, catalase-catalyzed decomposition of H_2O_2 enhances the diffusion of the nanomotors, leading to higher cellular uptake and further enhancing photodynamic and starvation therapeutic effects. Besides, the decomposition of H_2O_2 could generate more O_2 molecules, which help the generation of cytotoxic O_2 and the depletion of intracellular glucose, resulting in a more efficient PDT and ST through a positive feedback.[171]

Zhan *et al.*[172] have reported a facile one-step methodology using air bubbles as a template under mild conditions to synthesize polydopamine (PDA) nanobowls with tailored openings and holes (Fig. 12e). Furthermore, $Mn(CO)_5Br$ (COMn, gas fuel generator) was loaded on the PDA nanobowls to form a nanomotor to carry zinc phthalocyanine (ZnPc, photosensitive drug) (denoted PCZN) (Fig. 12f). COMn would be decomposed to release CO and form Mn^{2+} in the presence of H_2O_2. In addition, Mn^{2+} could catalyse the decomposition of endogenous H_2O_2 to produce O_2. Thus, PCZNs can be efficiently propelled by multi-gas fuels (CO and O_2) to enlarge the PS diffusion range and expand the O_2 reach to improve the PDT activity. In addition, PCZNs have multiple functions, including promoting drug accumulation at the tumor site, relieving tumor hypoxia, enabling synergistic therapy (PTT and PDT) and multimodal imaging, beneficial to effective cancer theranostics (Fig. 12g).[172]

Zhang *et al.*[173] have proposed a new strategy to improve the efficiency of photodynamic therapy. They loaded iron oxide nanoparticles (IONPs) inside the self-assembly stomatocytes-like structure of poly(ethylene glycol) block

polystyrene (PEG-*b*-PS) to prepare a nanomotor (denoted IP-NM), which could generate O_2 as propelling power by catalysing endogenous H_2O_2 decomposition (Fig. 12h). The hybrid nanomotors can be gathered in tumor tissues under a magnetic field owing to the magnetism of IONPs. After being trapped by cancer cells, IONPs can catalyse the decomposition of endogenous H_2O_2 to generate O_2 as propelling force for ISPNMs movement. The motion characteristics of ISPNMs expand the distribution of ZnPc to enlarge the ROS reactive distribution and enhance the activity of PDT. Furthermore, ISP-NMs have nuclear magnetic resonance imaging (MRI) function since IONPs are efficient T_2 contrast agents. Furthermore, O_2 inside cancer cells is insufficient and it is further consumed during the PDT process.

Conclusion and perspective

In this review, we have discussed the recent progress made in the artificially fabricated micro/nanomotors towards the diagnosis and treatment of life-threatening disease, cancer. The developed micro/nanomotors are being known as the "new generation multitasking asset", which can perform various tasks, such as diagnosis, imaging and targeted drug delivery in cancer therapeutics. The past decade has witnessed appreciable progress in the concepts, working mechanisms, design, fabrication, and diverse biomedical applications of micro/nanomotors. Prompt changes in the design and modes of operation of micro/nanomotors expand its feasibility for various practical biomedical applications. Advances have shown that the practical approach of micro/nanomotors has been improved remarkably with modifications in their basic characteristics such as control, speed, propulsion methods, nanomaterial combination and lifetime. In the early years, more research was focused on the theoretical approach of various types of micro/nanomotors. However, a more intensive research is being carried out by applying these micro/nanomotors practically, such as externally controlled biochemical release and cargo delivery. Although there are some challenges to be conquered for using these micro/nanomotors for the *in vivo* targeted drug delivery, recent innovations explored through bioinspiration regarding the design of smart micro/nanomotors could definitely be the fruitful step towards achieving precise treatment using nanomachine for accurate diagnosis and improved delivery of therapeutic agents in the human body for future nanomedicine.

Despite considerable advancement, micro/nanomotors still have many shortcomings to be addressed right before their practical implementation in our day-to-day lives. Most of the micro/nanomotors have been made up of nanometals, which show some corrosive and toxic effects on living cells. Therefore, the issue of the biocompatibility of using nanomotors for drug delivery applications should be taken into consideration. In addition, post completion of the delivery mission, these nanomotors must get self-degraded. Hence, biodegradability or excretion of nanomotors from the body needs to be focused. Furthermore, effective and long-term delivery of these nanomachines into the body with sufficient power/fuel across various barriers and detecting their exact location in the body should be investigated. It is mandatory to innovate various designs and fabricate nanomotors equipped with intelligence in such a way that they can operate very feasibly at the site of action and sense the surrounding environment, and simultaneously, where movement should take place. For instance, nanomotors facilitated with chemical or biological linkers (*e.g.*, protease enzyme and acidity), sensitive to the tumor micro-environment could be smart systems for faster diagnosis or treatment of diseases. Additional efforts should be given to developing a nanomachine, which can perform multiple functions for cellular uptake, diagnostic or theranostic. Moreover, it is also critical to develop a self-powered nanomachine for *in situ* alternate powering sources that can even face large blood drag.

As researchers' imagination and skills move toward furnishing these smaller devices with multifunctional entities, the exciting prospect of nanomachines would be achieved. With the collaborative efforts of multidisciplinary teams, we can surely envision that these fabricated nanomotors would provide new and unique assets as theranostic agents with both diagnostic and therapeutic functions such as drug carriers. Altogether, these incessant efforts in the exploration and advancement of micro/nanomotors are quite exciting towards getting the products such as intelligent nanorobots and nanomachines, which have been dreamed of and will manifest a huge impact on the quality of human lives.

Conflicts of interest

There are no conflicts to declare.

Acknowledgements

YNT would like to acknowledge the research support funding from the Newcastle University in Singapore (RSA/CCEAMD5010).

References

1 H. Sung, J. Ferlay, R. L. Siegel, M. Laversanne, I. Soerjomataram, A. Jemal and F. Bray, *Ca-Cancer J. Clin.*, 2021, **71**, 209–249.
2 J. Ferlay, I. Soerjomataram, R. Dikshit, S. Eser, C. Mathers, M. Rebelo, D. M. Parkin, D. Forman and F. Bray, *Int. J. Cancer*, 2015, **136**, E359–E386.
3 E. Assah, W. Goh, X. T. Zheng, T. X. Lim, J. Li, D. Lane, F. Ghadessy and Y. N. Tan, *Colloids Surf., B*, 2018, **169**, 214–221.
4 P. Chandra, Y. N. Tan and S. P. Singh, *Next generation point-of-care biomedical sensors technologies for cancer diagnosis*, Springer, 2017.

5 X. T. Zheng, W. L. Goh, P. Yeow, D. P. Lane, F. J. Ghadessy and Y. N. Tan, *Sens. Actuators, B*, 2019, **279**, 79–86.
6 B. A. Chabner and T. G. Roberts, *Nat. Rev. Cancer*, 2005, **5**, 65–72.
7 M. N. Alekshun and S. B. Levy, *Cell*, 2007, **128**, 1037–1050.
8 S. Lehtinen, F. Blanquart, N. J. Croucher, P. Turner, M. Lipsitch and C. Fraser, *Proc. Natl. Acad. Sci. U. S. A.*, 2017, **114**, 1075–1080.
9 M. Greaves and C. C. Maley, *Nature*, 2012, **481**, 306–313.
10 N. Murugaesu, S. K. Chew and C. Swanton, *Am. J. Pathol.*, 2013, **182**, 1962–1971.
11 F. D. S. E. Melo, L. Vermeulen, E. Fessler and J. P. Medema, *EMBO Rep.*, 2013, **14**, 686–695.
12 P. Eirew, A. Steif, J. Khattra, G. Ha, D. Yap, H. Farahani, K. Gelmon, S. Chia, C. Mar, A. Wan, E. Laks, J. Biele, K. Shumansky, J. Rosner, A. McPherson, C. Nielsen, A. J. L. Roth, C. Lefebvre, A. Bashashati, C. de Souza, C. Siu, R. Aniba, J. Brimhall, A. Oloumi, T. Osako, A. Bruna, J. L. Sandoval, T. Algara, W. Greenwood, K. Leung, H. Cheng, H. Xue, Y. Wang, D. Lin, A. J. Mungall, R. Moore, Y. Zhao, J. Lorette, L. Nguyen, D. Huntsman, C. J. Eaves, C. Hansen, M. A. Marra, C. Caldas, S. P. Shah and S. Aparicio, *Nature*, 2015, **518**, 422–426.
13 R. L. Randall, V. Lewis and K. Weber, *An Integrated Approach to Patient Care*, 2016, p. 2016.
14 R. Kang, P. P. Goodney and S. L. Wong, *J. Surg. Oncol.*, 2016, **114**, 275–280.
15 J. Xie, S. Lee and X. Chen, *Adv. Drug Delivery Rev.*, 2010, **62**, 1064–1079.
16 S. Sultana, M. R. Khan, M. Kumar, S. Kumar and M. Ali, *J. Drug Targeting*, 2013, **21**, 107–125.
17 A. Lajevardi, M. H. Sadr, M. T. Yaraki, A. Badiei and M. Armaghan, *New J. Chem.*, 2018, **42**, 9690–9701.
18 I. Akbarzadeh, M. T. Yaraki, M. Bourbour, H. Noorbazargan, A. Lajevardi, S. M. S. Shilsar, F. Heidari and S. M. Mousavian, *J. Drug Delivery Sci. Technol.*, 2020, **57**, 101715.
19 I. Akbarzadeh, M. T. Yaraki, S. Ahmadi, M. Chiani and D. Nourouzian, *Adv. Powder Technol.*, 2020, **31**, 4064–4071.
20 R. Ghafelehbashi, I. Akbarzadeh, M. T. Yaraki, A. Lajevardi, M. Fatemizadeh and L. Heidarpoor Saremi, *Int. J. Pharm.*, 2019, **569**, 118580.
21 T. F. Martens, K. Remaut, J. Demeester, S. C. De Smedt and K. Braeckmans, *Nano Today*, 2014, **9**, 344–364.
22 N. Hirokawa, Y. Noda, Y. Tanaka and S. Niwa, *Nat. Rev. Mol. Cell Biol.*, 2009, **10**, 682–696.
23 C. Veigel and C. F. Schmidt, *Nat. Rev. Mol. Cell Biol.*, 2011, **12**, 163–176.
24 Z. Wu, J. Li, B. E.-F. de Ávila, T. Li, W. Gao, Q. He, L. Zhang and J. Wang, *Adv. Funct. Mater.*, 2015, **25**, 7497–7501.
25 Z. Wu, Y. Wu, W. He, X. Lin, J. Sun and Q. He, *Angew. Chem., Int. Ed.*, 2013, **52**, 7000–7003.
26 Z. Lin, C. Gao, D. Wang and Q. He, *Angew. Chem., Int. Ed.*, 2021, **60**, 8750–8754.
27 H. Zhang, Z. Li, C. Gao, X. Fan, Y. Pang, T. Li, Z. Wu, H. Xie and Q. He, *Sci. Robot.*, 2021, **6**, 9519eaaz.
28 W. Xi, A. A. Solovev, A. N. Ananth, D. H. Gracias, S. Sanchez and O. G. Schmidt, *Nanoscale*, 2013, **5**, 1294–1297.
29 S. Balasubramanian, D. Kagan, C.-M. J. Hu, S. Campuzano, M. J. Lobo-Castañon, N. Lim, D. Y. Kang, M. Zimmerman, L. Zhang and J. Wang, *Angew. Chem., Int. Ed.*, 2011, **50**, 4161–4164.
30 F. Peng, Y. Tu, A. Adhikari, J. C. J. Hintzen, D. W. P. M. Löwik and D. A. Wilson, *Chem. Commun.*, 2017, **53**, 1088–1091.
31 T. Patino, A. Porchetta, A. Jannasch, A. Lladó, T. Stumpp, E. Schäffer, F. Ricci and S. Sánchez, *Nano Lett.*, 2019, **19**, 3440–3447.
32 J. Li, P. Angsantikul, W. Liu, B. E.-F. de Ávila, S. Thamphiwatana, M. Xu, E. Sandraz, X. Wang, J. Delezuk, W. Gao, L. Zhang and J. Wang, *Angew. Chem., Int. Ed.*, 2017, **56**, 2156–2161.
33 K. Xiong, L. Xu, J. Lin, F. Mou and J. Guan, *Research*, 2020, **2020**, 6213981.
34 X. Lin, B. Xu, H. Zhu, J. Liu, A. Solovev and Y. Mei, *Research*, 2020, **2020**, 7659749.
35 K. Hou, Y. Zhang, M. Bao, Y. Liu, J. Wang, C. Xin, Z. Wei, H. Zhang, Z. Wu and Z. Wang, *Mater. Adv.*, 2021, **2**, 3441–3458.
36 H. Choi, B. W. Hwang, K. M. Park, K. S. Kim and S. K. Hahn, *Part. Part. Syst. Charact.*, 2020, **37**, 1900418.
37 J. L. Anderson, *Annu. Rev. Fluid Mech.*, 1989, **21**, 61–99.
38 W. F. Paxton, K. C. Kistler, C. C. Olmeda, A. Sen, S. K. St. Angelo, Y. Cao, T. E. Mallouk, P. E. Lammert and V. H. Crespi, *J. Am. Chem. Soc.*, 2004, **126**, 13424–13431.
39 P. M. Wheat, N. A. Marine, J. L. Moran and J. D. Posner, *Langmuir*, 2010, **26**, 13052–13055.
40 X. Ma, J. Katuri, Y. Zeng, Y. Zhao and S. Sanchez, *Small*, 2015, **11**, 5023–5027.
41 R. A. Pavlick, S. Sengupta, T. McFadden, H. Zhang and A. Sen, *Angew. Chem., Int. Ed.*, 2011, **50**, 9374–9377.
42 N. Chaturvedi, Y. Hong, A. Sen and D. Velegol, *Langmuir*, 2010, **26**, 6308–6313.
43 Y. Gao, R. P. A. Dullens and D. G. A. L. Aarts, *Soft Matter*, 2018, **14**, 7119–7125.
44 M. E. Ibele, P. E. Lammert, V. H. Crespi and A. Sen, *ACS Nano*, 2010, **4**, 4845–4851.
45 J. G. Gibbs and Y. P. Zhao, *Appl. Phys. Lett.*, 2009, **94**, 163104.
46 W. Gao, A. Uygun and J. Wang, *J. Am. Chem. Soc.*, 2012, **134**, 897–900.
47 W. Gao, A. Uygun and J. Wang, *J. Am. Chem. Soc.*, 2012, **134**, 897–900.
48 M. Ren, W. Guo, H. Guo and X. Ren, *ACS Appl. Mater. Interfaces*, 2019, **11**, 22761–22767.
49 W. Wang, W. Duan, S. Ahmed, T. E. Mallouk and A. Sen, *Nano Today*, 2013, **8**, 531–554.
50 S. Wang and N. Wu, *Langmuir*, 2014, **30**, 3477–3486.
51 H.-R. Jiang, N. Yoshinaga and M. Sano, *Phys. Rev. Lett.*, 2010, **105**, 268302.
52 W. Qin, T. Peng, Y. Gao, F. Wang, X. Hu, K. Wang, J. Shi, D. Li, J. Ren and C. Fan, *Angew. Chem., Int. Ed.*, 2017, **56**, 515–518.
53 Z. Wu, T. Si, W. Gao, X. Lin, J. Wang and Q. He, *Small*, 2016, **12**, 577–582.
54 W. Wang, L. A. Castro, M. Hoyos and T. E. Mallouk, *ACS Nano*, 2012, **6**, 6122–6132.

55 F. Kümmel, B. ten Hagen, R. Wittkowski, I. Buttinoni, R. Eichhorn, G. Volpe, H. Löwen and C. Bechinger, *Phys. Rev. Lett.*, 2013, **110**, 198302.
56 X. Ma, A. Jannasch, U.-R. Albrecht, K. Hahn, A. Miguel-López, E. Schäffer and S. Sánchez, *Nano Lett.*, 2015, **15**, 7043–7050.
57 H. Zhang, W. Duan, M. Lu, X. Zhao, S. Shklyaev, L. Liu, T. J. Huang and A. Sen, *ACS Nano*, 2014, **8**, 8537–8542.
58 X. Ma, X. Wang, K. Hahn and S. Sánchez, *ACS Nano*, 2016, **10**, 3597–3605.
59 G. Roosen and C. Imbert, *Phys. Lett. A*, 1976, **59**, 6–8.
60 B. Qian, D. Montiel, A. Bregulla, F. Cichos and H. Yang, *Chem. Sci.*, 2013, **4**, 1420–1429.
61 W. Gao, S. Sattayasamitsathit, K. M. Manesh, D. Weihs and J. Wang, *J. Am. Chem. Soc.*, 2010, **132**, 14403–14405.
62 S. Tottori, L. Zhang, F. Qiu, K. K. Krawczyk, A. Franco-Obregón and B. J. Nelson, *Adv. Mater.*, 2012, **24**, 811–816.
63 P. Calvo-Marzal, S. Sattayasamitsathit, S. Balasubramanian, J. R. Windmiller, C. Dao and J. Wang, *Chem. Commun.*, 2010, **46**, 1623–1624.
64 W. Gao, A. Pei and J. Wang, *ACS Nano*, 2012, **6**, 8432–8438.
65 D.-D. Qin, Y.-P. Bi, X.-J. Feng, W. Wang, G. D. Barber, T. Wang, Y.-M. Song, X.-Q. Lu and T. E. Mallouk, *Chem. Mater.*, 2015, **27**, 4180–4183.
66 W. Liu, H. Ge, X. Chen, X. Lu, Z. Gu, J. Li and J. Wang, *ACS Appl. Mater. Interfaces*, 2019, **11**, 16164–16173.
67 T. Patiño, N. Feiner-Gracia, X. Arqué, A. Miguel-López, A. Jannasch, T. Stumpp, E. Schäffer, L. Albertazzi and S. Sánchez, *J. Am. Chem. Soc.*, 2018, **140**, 7896–7903.
68 P. A. Hassan, S. Rana and G. Verma, *Langmuir*, 2015, **31**, 3–12.
69 J. A. Gallego-Urrea, J. Tuoriniemi and M. Hassellöv, *TrAC, Trends Anal. Chem.*, 2011, **30**, 473–483.
70 Y. Peng, B. Xiong, L. Peng, H. Li, Y. He and E. S. Yeung, *Anal. Chem.*, 2015, **87**, 200–215.
71 N. Seow, Y. N. Tan and L.-Y. L. Yung, *Part. Part. Syst. Charact.*, 2014, **31**, 1260–1268.
72 J. Li, W. Liu, J. Wang, I. Rozen, S. He, C. Chen, H. G. Kim, H.-J. Lee, H.-B.-R. Lee, S.-H. Kwon, T. Li, L. Li, J. Wang and Y. Mei, *Adv. Funct. Mater.*, 2017, **27**, 1700598.
73 O. Felfoul, J. Mathieu, G. Beaudoin and S. Martel, *IEEE Trans. Med. Imaging*, 2008, **27**, 28–35.
74 S. A. Soper, K. Brown, A. Ellington, B. Frazier, G. Garcia-Manero, V. Gau, S. I. Gutman, D. F. Hayes, B. Korte, J. L. Landers, D. Larson, F. Ligler, A. Majumdar, M. Mascini, D. Nolte, Z. Rosenzweig, J. Wang and D. Wilson, *Biosens. Bioelectron.*, 2006, **21**, 1932–1942.
75 N. L. Henry and D. F. Hayes, *Mol. Oncol.*, 2012, **6**, 140–146.
76 A. Chałupniak, E. Morales-Narváez and A. Merkoçi, *Adv. Drug Delivery Rev.*, 2015, **95**, 104–116.
77 X. Liu, H. Jiang, Y. Fang, W. Zhao, N. Wang and G. Zang, *Anal. Chem.*, 2015, **87**, 9163–9169.
78 G. Nie, C. Li, L. Zhang and L. Wang, *J. Mater. Chem. B*, 2014, **2**, 8321–8328.
79 C.-Y. Wen, H.-Y. Xie, Z.-L. Zhang, L.-L. Wu, J. Hu, M. Tang, M. Wu and D.-W. Pang, *Nanoscale*, 2016, **8**, 12406–12429.
80 H. Wang and M. Pumera, *Adv. Funct. Mater.*, 2018, **28**, 1705421.
81 A. de Gramont, S. Watson, L. M. Ellis, J. Rodón, J. Tabernero, A. de Gramont and S. R. Hamilton, *Nat. Rev. Clin. Oncol.*, 2015, **12**, 197–212.
82 S. K. Gupta, A. Foinquinos, S. Thum, J. Remke, K. Zimmer, C. Bauters, P. de Groote, R. A. Boon, L. J. de Windt, S. Preissl, L. Hein, S. Batkai, F. Pinet and T. Thum, *J. Am. Coll. Cardiol.*, 2016, **68**, 1557–1571.
83 M. Tavakkoli Yaraki and Y. N. Tan, *Sens. Int.*, 2020, **1**, 100049.
84 X. T. Zheng and Y. N. Tan, *Sens. Int.*, 2020, **1**, 100034.
85 Y. N. Tan, K. H. Lee and X. Su, *Anal. Chem.*, 2011, **83**, 4251–4257.
86 Y. N. Tan, X. Su, Y. Zhu and J. Y. Lee, *ACS Nano*, 2010, **4**, 5101–5110.
87 Y. N. Tan, X. Su, E. T. Liu and J. S. Thomsen, *Anal. Chem.*, 2010, **82**, 2759–2765.
88 V. X. T. Zhao, T. I. Wong, X. T. Zheng, Y. N. Tan and X. Zhou, *Mater. Sci. Energy Technol.*, 2020, **3**, 237–249.
89 Y. N. Tan, K. H. Lee and X. Su, *RSC Adv.*, 2013, **3**, 21604–21612.
90 N. Seow, Y. N. Tan, L.-Y. L. Yung and X. Su, *Sci. Rep.*, 2015, **5**, 18293.
91 Y. Yu, B. Y. L. Mok, X. J. Loh and Y. N. Tan, *Adv. Healthcare Mater.*, 2016, **5**, 1844–1859.
92 Y. Yu, S. Y. New, J. Xie, X. Su and Y. N. Tan, *Chem. Commun.*, 2014, **50**, 13805–13808.
93 H. V. Xu, Y. Zhao and Y. N. Tan, *ACS Appl. Mater. Interfaces*, 2019, **11**, 27233–27242.
94 M. T. Yaraki and Y. N. Tan, *Chem. – Asian J.*, 2020, **15**, 3180–3208.
95 W.-H. Chen, W.-C. Liao, Y. S. Sohn, M. Fadeev, A. Cecconello, R. Nechushtai and I. Willner, *Adv. Funct. Mater.*, 2018, **28**, 1705137.
96 X. Xue, W. Xu, F. Wang and X. Liu, *J. Am. Chem. Soc.*, 2009, **131**, 11668–11669.
97 H. V. Xu, X. T. Zheng, B. Y. L. Mok, S. A. Ibrahim, Y. Yu and Y. N. Tan, *J. Mol. Eng. Mater.*, 2016, **04**, 1640003.
98 D. F. Báez, G. Ramos, A. Corvalán, M. L. Cordero, S. Bollo and M. J. Kogan, *Sens. Actuators, B*, 2020, **310**, 127843.
99 X. Zhang, C. Chen, J. Wu and H. Ju, *ACS Appl. Mater. Interfaces*, 2019, **11**, 13581–13588.
100 W. Goh, E. Assah, X. Zheng, D. Lane, F. Ghadessy and Y. Tan, in *Next Generation Point-of-care Biomedical Sensors Technologies for Cancer Diagnosis*, Springer, 2017, pp. 31–58.
101 X. Yu, Y. Li, J. Wu and H. Ju, *Anal. Chem.*, 2014, **86**, 4501–4507.
102 P. Xu, Y. Yu, T. Li, H. Chen, Q. Wang, M. Wang, M. Wan and C. Mao, *Anal. Chim. Acta*, 2020, **1129**, 60–68.
103 M. A. Tabrizi, M. Shamsipur, R. Saber and S. Sarkar, *Biosens. Bioelectron.*, 2018, **110**, 141–146.
104 P. L. Venugopalan, B. E.-F. de Ávila, M. Pal, A. Ghosh and J. Wang, *ACS Nano*, 2020, **14**, 9423–9439.
105 J. Geng, W. L. Goh, C. Zhang, D. P. Lane, B. Liu, F. Ghadessy and Y. N. Tan, *J. Mater. Chem. B*, 2015, **3**, 5933–5937.

106 M. Beltrán-Gastélum, B. E.-F. de Ávila, H. Gong, P. L. Venugopalan, T. Hianik, J. Wang and V. Subjakova, *ChemPhysChem*, 2019, **20**, 3177–3180.
107 B. E.-F. de Ávila, A. Martín, F. Soto, M. A. Lopez-Ramirez, S. Campuzano, G. M. Vásquez-Machado, W. Gao, L. Zhang and J. Wang, *ACS Nano*, 2015, **9**, 6756–6764.
108 Z. Wu, X. Lin, Y. Wu, T. Si, J. Sun and Q. He, *ACS Nano*, 2014, **8**, 6097–6105.
109 J. Sun, M. Mathesh, W. Li and D. A. Wilson, *ACS Nano*, 2019, **13**, 10191–10200.
110 M. Beltrán-Gastélum, B. E.-F. de Ávila, H. Gong, P. L. Venugopalan, T. Hianik, J. Wang and V. Subjakova, *ChemPhysChem*, 2019, **20**, 3177–3180.
111 J. R. Qualliotine, G. Bolat, M. Beltrán-Gastélum, B. E.-F. de Ávila, J. Wang and J. A. Califano, *Otolaryngol.–Head Neck Surg.*, 2019, **161**, 814–822.
112 J. Wu, S. Balasubramanian, D. Kagan, K. M. Manesh, S. Campuzano and J. Wang, *Nat. Commun.*, 2010, **1**, 36.
113 K. Van Nguyen and S. D. Minteer, *Chem. Commun.*, 2015, **51**, 4782–4784.
114 C. Gao, Y. Wang, Z. Ye, Z. Lin, X. Ma and Q. He, *Adv. Mater.*, 2020, 2000512.
115 J. Wang, R. Dong, H. Wu, Y. Cai and B. Ren, *Nano-Micro Lett.*, 2019, **12**, 11.
116 J. Condeelis and R. Weissleder, *Cold Spring Harbor Perspect. Biol.*, 2010, **2**, a003848.
117 X. Yan, Q. Zhou, M. Vincent, Y. Deng, J. Yu, J. Xu, T. Xu, T. Tang, L. Bian, Y.-X. J. Wang, K. Kostarelos and L. Zhang, *Sci. Robot.*, 2017, **2**, eaaq1155.
118 Á. Molinero-Fernández, M. Moreno-Guzmán, L. Arruza, M. Á. López and A. Escarpa, *ACS Sens.*, 2020, **5**, 1336–1344.
119 D. Vilela, U. Cossío, J. Parmar, A. M. Martínez-Villacorta, V. Gómez-Vallejo, J. Llop and S. Sánchez, *ACS Nano*, 2018, **12**, 1220–1227.
120 A. Aziz, S. Pane, V. Iacovacci, N. Koukourakis, J. Czarske, A. Menciassi, M. Medina-Sánchez and O. G. Schmidt, *ACS Nano*, 2020, **14**, 10865–10893.
121 Z. Wu, L. Li, Y. Yang, P. Hu, Y. Li, S.-Y. Yang, L. V. Wang and W. Gao, *Sci. Robot.*, 2019, **4**, eaax0613.
122 B. Wang, Y. Zhang and L. Zhang, *Quant. Imaging. Med. Surg.*, 2018, **8**, 461–479.
123 J. Guo, J. J. Gallegos, A. R. Tom and D. Fan, *ACS Nano*, 2018, **12**, 1179–1187.
124 M. R. Benoit, D. Mayer, Y. Barak, I. Y. Chen, W. Hu, Z. Cheng, S. X. Wang, D. M. Spielman, S. S. Gambhir and A. Matin, *Clin. Cancer Res.*, 2009, **15**, 5170–5177.
125 Z. Wu, B. E.-F. de Ávila, A. Martín, C. Christianson, W. Gao, S. K. Thamphiwatana, A. Escarpa, Q. He, L. Zhang and J. Wang, *Nanoscale*, 2015, **7**, 13680–13686.
126 Y. Yu, J. Geng, E. Y. X. Ong, V. Chellappan and Y. N. Tan, *Adv. Healthcare Mater.*, 2016, **5**, 2528–2535.
127 X. T. Zheng, Y. C. Lai and Y. N. Tan, *Nanoscale Adv.*, 2019, **1**, 2250–2257.
128 H. V. Xu, X. T. Zheng, Y. Zhao and Y. N. Tan, *ACS Appl. Mater. Interfaces*, 2018, **10**, 19881–19888.
129 M. T. Yaraki, S. D. Rezaei and Y. N. Tan, *Phys. Chem. Chem. Phys.*, 2020, **22**, 5673–5687.
130 M. T. Yaraki, Y. Pan, F. Hu, Y. Yu, B. Liu and Y. N. Tan, *Mater. Chem. Front.*, 2020, **4**, 3074–3085.
131 Y. Choi, X. T. Zheng and Y. N. Tan, *Mol. Syst. Des. Eng.*, 2020, **5**, 67–90.
132 M. T. Yaraki, F. Hu, S. D. Rezaei, B. Liu and Y. N. Tan, *Nanoscale Adv.*, 2020, **2**, 2859–2869.
133 X. T. Zheng and Y. N. Tan, *Small*, 2020, **16**, 1903328.
134 J. Y. C. Lim, Y. Yu, G. Jin, K. Li, Y. Lu, J. Xie and Y. N. Tan, *Nanoscale Adv.*, 2020, **2**, 3921–3932.
135 M. Saraf, M. T. Yaraki, Prateek, Y. N. Tan and R. K. Gupta, *ACS Appl. Nano Mater.*, 2021, **4**, 911–948.
136 M. T. Yaraki, M. Wu, E. Middha, W. Wu, S. D. Rezaei, B. Liu and Y. N. Tan, *Nano-Micro Lett.*, 2021, **13**, 58.
137 J. Rao, A. Dragulescu-Andrasi and H. Yao, *Curr. Opin. Biotechnol.*, 2007, **18**, 17–25.
138 M. Wan, H. Chen, Q. Wang, Q. Niu, P. Xu, Y. Yu, T. Zhu, C. Mao and J. Shen, *Nat. Commun.*, 2019, **10**, 966.
139 P. Zhang, L. Li, L. Lin, J. Shi and L. V. Wang, *Light: Sci. Appl.*, 2019, **8**, 36.
140 M. Sun, X. Fan, X. Meng, J. Song, W. Chen, L. Sun and H. Xie, *Nanoscale*, 2019, **11**, 18382–18392.
141 B. Khezri, S. M. B. Mousavi, L. Krejčová, Z. Heger, Z. Sofer and M. Pumera, *Adv. Funct. Mater.*, 2019, **29**, 1806696.
142 S. Wilhelm, A. J. Tavares, Q. Dai, S. Ohta, J. Audet, H. F. Dvorak and W. C. W. Chan, *Nat. Rev. Mater.*, 2016, **1**, 16014.
143 M. J. Ernsting, M. Murakami, A. Roy and S.-D. Li, *J. Controlled Release*, 2013, **172**, 782–794.
144 H. Chen, Z. Gu, H. An, C. Chen, J. Chen, R. Cui, S. Chen, W. Chen, X. Chen, X. Chen, Z. Chen, B. Ding, Q. Dong, Q. Fan, T. Fu, D. Hou, Q. Jiang, H. Ke, X. Jiang, G. Liu, S. Li, T. Li, Z. Liu, G. Nie, M. Ovais, D. Pang, N. Qiu, Y. Shen, H. Tian, C. Wang, H. Wang, Z. Wang, H. Xu, J.-F. Xu, X. Yang, S. Zhu, X. Zheng, X. Zhang, Y. Zhao, W. Tan, X. Zhang and Y. Zhao, *Sci. China: Chem.*, 2018, **61**, 1503–1552.
145 X. Liang, C. Gao, L. Cui, S. Wang, J. Wang and Z. Dai, *Adv. Mater.*, 2017, **29**, 1703135.
146 M. O. Palumbo, P. Kavan, W. Miller, L. Panasci, S. Assouline, N. Johnson, V. Cohen, F. Patenaude, M. Pollak and R. T. Jagoe, *Front. Pharmacol.*, 2013, **4**, 57.
147 M. Zhou, T. Hou, J. Li, S. Yu, Z. Xu, M. Yin, J. Wang and X. Wang, *ACS Nano*, 2019, **13**, 1324–1332.
148 V. Magdanz, M. Medina-Sánchez, Y. Chen, M. Guix and O. G. Schmidt, *Adv. Funct. Mater.*, 2015, **25**, 2763–2770.
149 H. Xu, M. Medina-Sanchez, D. R. Brison, R. J. Edmondson, S. S. Taylor, L. Nelson, K. Zeng, S. Bagley, C. Ribeiro and L. P. Restrepo, 2019, arXiv preprint arXiv:1904.12684.
150 N. F. Rosli, C. C. Mayorga-Martinez, A. C. Fisher, O. Alduhaish, R. D. Webster and M. Pumera, *Appl. Mater. Today*, 2020, **21**, 100819.
151 K. Liu, J. Ou, S. Wang, J. Gao, L. Liu, Y. Ye, D. A. Wilson, Y. Hu, F. Peng and Y. Tu, *Appl. Mater. Today*, 2020, **20**, 100694.
152 J. A. Tejeda-Rodríguez, A. Núñez, F. Soto, V. García-Gradilla, R. Cadena-Nava, J. Wang and R. Vazquez-Duhalt, *ChemNanoMat*, 2019, **5**, 194–200.

153 Z. Jin, K. T. Nguyen, G. Go, B. Kang, H.-K. Min, S.-J. Kim, Y. Kim, H. Li, C.-S. Kim, S. Lee, S. Park, K.-P. Kim, K. M. Huh, J. Song, J.-O. Park and E. Choi, *Nano Lett.*, 2019, **19**, 8550–8564.
154 B. Wu, J. Fu, Y. Zhou, S. Luo, Y. Zhao, G. Quan, X. Pan and C. Wu, *Acta Pharm. Sin. B*, 2020, **10**, 2198–2211.
155 M. Zhou, Y. Xing, X. Li, X. Du, T. Xu and X. Zhang, *Small*, 2020, **16**, 2003834.
156 Y. Yu, W. D. Lee and Y. N. Tan, *Mater. Sci. Eng., C*, 2020, **109**, 110525.
157 K. Deng, C. Li, S. Huang, B. Xing, D. Jin, Q. Zeng, Z. Hou and J. Lin, *Small*, 2017, **13**, 1702299.
158 H. Sun, S. Li, W. Qi, R. Xing, Q. Zou and X. Yan, *Colloids Surf., A*, 2018, **538**, 795–801.
159 K. M. Harmatys, M. Overchuk and G. Zheng, *Acc. Chem. Res.*, 2019, **52**, 1265–1274.
160 X. Song, Q. Chen and Z. Liu, *Nano Res.*, 2015, **8**, 340–354.
161 H. Choi, G.-H. Lee, K. S. Kim and S. K. Hahn, *ACS Appl. Mater. Interfaces*, 2018, **10**, 2338–2346.
162 J. Shao, S. Cao, D. S. Williams, L. K. E. A. Abdelmohsen and J. C. M. van Hest, *Angew. Chem., Int. Ed.*, 2020, **59**, 16918–16925.
163 M. Xuan, J. Shao, C. Gao, W. Wang, L. Dai and Q. He, *Angew. Chem., Int. Ed.*, 2018, **57**, 12463–12467.
164 M. Xuan, J. Shao, L. Dai, J. Li and Q. He, *ACS Appl. Mater. Interfaces*, 2016, **8**, 9610–9618.
165 P.-P. Yang, Y.-G. Zhai, G.-B. Qi, Y.-X. Lin, Q. Luo, Y. Yang, A.-P. Xu, C. Yang, Y.-S. Li, L. Wang and H. Wang, *Small*, 2016, **12**, 5423–5430.
166 D. E. J. G. J. Dolmans, D. Fukumura and R. K. Jain, *Nat. Rev. Cancer*, 2003, **3**, 380–387.
167 A. P. Castano, P. Mroz and M. R. Hamblin, *Nat. Rev. Cancer*, 2006, **6**, 535–545.
168 C. Gao, Z. Lin, D. Wang, Z. Wu, H. Xie and Q. He, *ACS Appl. Mater. Interfaces*, 2019, **11**, 23392–23400.
169 B. Wu, J. Fu, Y. Zhou, S. Luo, Y. Zhao, G. Quan, X. Pan and C. Wu, *Acta Pharm. Sin. B*, 2020, **10**, 2198–2211.
170 D. Xu, C. Zhou, C. Zhan, Y. Wang, Y. You, X. Pan, J. Jiao, R. Zhang, Z. Dong, W. Wang and X. Ma, *Adv. Funct. Mater.*, 2019, **29**, 1807727.
171 Y. You, D. Xu, X. Pan and X. Ma, *Appl. Mater. Today*, 2019, **16**, 508–517.
172 Q. Zhan, X. Shi, D. Fan, L. Zhou and S. Wei, *Chem. Eng. J.*, 2021, **404**, 126443.
173 P. Zhang, G. Wu, C. Zhao, L. Zhou, X. Wang and S. Wei, *Colloids Surf., B*, 2020, **194**, 111204.